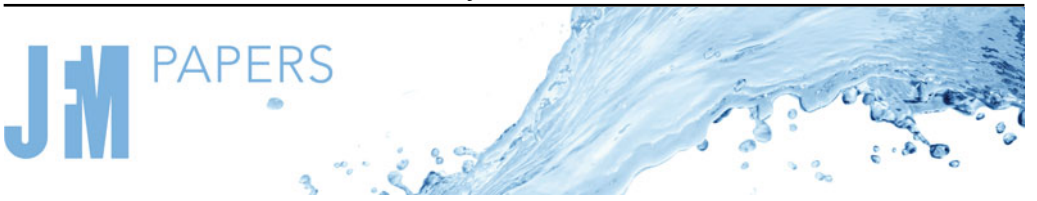
J. Fluid Mech. (2025), *vol.* 1022, A29, doi:10.1017/jfm.2025.10740



Analytical model of the linear Richtmyer–Meshkov instability when a shock is reflected

Juan Gustavo Wouchuk

University of Castilla La Mancha, Ciudad Real, Spain (retired)

Corresponding author: Juan Gustavo Wouchuk, gustavo.wouchuk@uclm.es

(Received 5 April 2025; revised 24 July 2025; accepted 16 September 2025)

The Richtmyer–Meshkov instability (RMI) develops when a planar shock front hits a rippled contact surface separating two different fluids. After the incident shock refraction, a transmitted shock is always formed and another shock or a rarefaction is reflected back. The pressure/entropy/vorticity fields generated by the rippled wavefronts are responsible of the generation of hydrodynamic perturbations in both fluids. In linear theory, the contact surface ripple reaches an asymptotic normal velocity which is dependent on the incident shock Mach number, fluid density ratio and compressibilities. In this work we only deal with the situations in which a shock is reflected. Our main goal is to show an explicit, closed form expression of the asymptotic linear velocity of the corrugation at the contact surface, valid for arbitrary Mach number, fluid compressibilities and pre-shock density ratio. An explicit analytical formula (closed form expression) is presented that works quite well in both limits: weak and strong incident shocks. The new formula is obtained by approximating the contact surface by a rigid piston. This work is a natural continuation of J. G. Wouchuk (2001 *Phys. Rev. E* vol. 63, p. 056303) and J. G. Wouchuk (2025 *Phys. Rev. E* vol. 111, p. 035102). It is shown here that a rigid piston approximation (RPA) works quite well in the general case, giving reasonable agreement with existing simulations, previous analytical models and experiments. An estimate of the relative error incurred because of the RPA is shown as a function of the incident shock Mach number M_i and ratio of γ values at the contact surface. The limits of validity of this approximation are also discussed. The calculations shown here have been done with the scientific software Mathematica. The files used to do these calculations can be retrieved as Supplemental Files to this article.

Key words: shock waves, instability control, supersonic flow

https://doi.org/10.1017/jfm.2025.10740 Published online by Cambridge University Press

© The Author(s), 2025. Published by Cambridge University Press.

1. Introduction

The Richtmyer–Meshkov instability (RMI) occurs at the rippled surface of separation between two fluids when a planar shock wave comes from one side and hits the contact surface (Richtmyer 1960; Meshkov 1969; Mikaelian 1991; Wouchuk & Nishihara 1996). This instability has been extensively studied together with its counterpart, the Rayleigh Taylor instability (RTI) due to their influence on the success of inertial confinement fusion (ICF) implosions (Ye Zhou 2017). After the incident shock refraction, two wave fronts are generated, one at each side of the material surface. A shock is always transmitted but, depending on the thermodynamic properties of both fluids, another shock or a centred rarefaction wave may be reflected back (Yang, Zhang & Sharp 1994). The reflected and transmitted wavefronts are also corrugated and, due to the conservation of tangential momentum at the wavefronts, an initial velocity circulation is created on the material surface. The spatially modulated tangential velocity at the ripple induces a pressure gradient along that surface which is responsible for the initial ripple acceleration. As the wavefronts propagate inside both fluids and their ripples oscillate in a damped fashion, a sound wave field is radiated towards the contact surface, which in turn modifies the velocity field near the surface ripple. As a result, the material interface corrugation grows in time and its normal velocity increases. For very small values of the corrugation amplitude compared with the perturbation wavelength, the surface ripple normal velocity usually reaches an asymptotic value (which will be also called the terminal velocity), after some gentle oscillations (Richtmyer 1960; Meshkov 1969; Fraley 1986; Mikaelian 1991; Yang *et al.* 1994; Velikovich *et al.* 2000; Wouchuk 2001*a*, 2001*b*). Later, as the surface ripple amplitude becomes comparable to the perturbation wavelength (Vandenboomgaerde *et al.* 2014), the instability enters the nonlinear regime and the growth velocity decreases in time due to nonlinear effects. The RMI instability growth in linear theory has been studied in the past for both cases in which a shock (Richtmyer 1960; Fraley 1986; Yang *et al.* 1994) or a rarefaction is reflected at the contact surface (Yang *et al.* 1994; Velikovich 1996). The RMI is an important phenomenon in ICF, because thermonuclear targets are never perfectly spherical and/or laser irradiation is non-uniform in general. To reach ignition conditions, an ICF target must be compressed in such a way that a central hot spot forms in the centre at the end of the implosion process. Let us briefly review the conditions for a successful implosion leading to high energy gain. The main objective is to form a central spot with high enough temperatures ($\sim$15 keV) in order to initiate fusion reactions. This central hot spot must be surrounded by colder fuel with its density properly shaped in space in such a way that that the alpha particles emitted from the centre will be absorbed by the surrounding, colder fuel, thereby increasing its temperature to finally ignite the whole fuel. Details may be found in Piriz and Wouchuk (1992), Lindl *et al.* (2014) and references therein. In order to reach these conditions of ignition, symmetry of the implosion is crucial. If the implosion proceeds non-uniformly, the central hot spot will not be formed and the energy gain will be drastically reduced. The irradiation of the outer surface is usually accomplished by means of an irradiation prepulse, followed by the main pulse, or even more complicated shapes. This sequence is necessary in order to shape the entropy of the fuel adequately creating a spot surrounded by colder fuel with properly shaped density in space. The main pulse is needed to later heat the central spot such that it reaches the temperatures needed for self-ignition. For more specific details, the reader is referred to Piriz and Wouchuk (1992), Lindl *et al.* (2014) and references therein. Typically, the spherical target is composed of several layers of different materials. Usually, the boundaries between the successive layers are not perfectly spherical, because of inherent non-uniformities during target manufacturing (Velikovich *et al.* 2020).

https://doi.org/10.1017/jfm.2025.10740 Published online by Cambridge University Press

This characteristic create a serious problem as to the uniformity of the implosion: when the first shock crosses any of the boundaries between successive layers, it may trigger the RMI at each material interface. The RMI growth will then ensue, which might rapidly enter its nonlinear phase. Things worsen immediately upon arrival of the second stronger shock (generated by the main pulse). This second wave will reshock the already existing hydrodynamic perturbations thereby increasing the rate at which the materials on each side of the interface mix with each other. As for the physics of re-shock, the interested reader is referred to the numerical study of Latini *et al.* (2007) and the recent experimental work of Cao *et al.* (2024) The overall picture worsens when taking into account that at each material surface there will be a whole spectrum of initial corrugations, which, after entering the nonlinear stage of growth, might become turbulent, seriously damaging target uniformity. Even worse is the fact that these hydrodynamic perturbations will serve as seeds for the later, more deleterious RTI, which may disrupt the target (RTI growth is exponential in time); see Ye Zhou (2017). A legitimate and totally justified question then arises: In which way could theoretical models like the one presented here help in the design of ICF experiments in order to mitigate instability growth as much as possible?

To answer this important question, it is convenient to recall another aspect of the RMI that may be of help. In Mikaelian (1991) predicted the possibility of stopping the growth of the RMI thanks to freeze-out. This phenomenon was later confirmed in Wouchuk & Nishihara (2004) for the shock reflected case by means of the compressible linear theory developed in Wouchuk (2001*a*), and for the rarefaction reflected case in Wouchuk & Sano (2015). It is noted that freeze-out is independent of the perturbation wavelength. Hence, if conditions are adequate for freeze-out, none the perturbation wavelengths imprinted on the surface will grow. Therefore, a whole multi-mode spectrum may be frozen out and it will not grow turbulently. Hence, there is the possibility that, if the properties of the materials (densities and isentropic exponents) are conveniently chosen, RMI growth at each boundary might be totally suppressed. The exact calculation of the freeze-out conditions is only possible with full compressible calculations as developed in Wouchuk (2001*a*) and Wouchuk & Sano (2015). Thus, linear calculations like the ones presented here may be useful to benchmark the hydrocodes used in ICF, and assist in the design of more robust thermonuclear targets.

There is still another important pay off for analytic linear compressible models. Nonlinear calculations, like those shown in Matsuoka *et al.* (2003, 2020) and Matsuoka & Nishihara (2023) are usually done once the perturbation velocity field has become incompressible. Still, the calculations of Matsuoka *et al.* (2003, 2020), Matsuoka & Nishihara (2023) need to be initialised with data from the compressible linear stage. Thus, calculations like the ones presented here may be useful to calculate the nonlinear evolution of the RMI in conditions relevant to ICF, and/or help in the design of successful target implosions, whether because they help finding realistic freeze-out conditions, or because they are used to initialise the complicated calculations of nonlinear models like the Vortex Sheet Model of Matsuoka *et al.* (2020) .

The main purpose of the present work is to derive a tractable, albeit approximate, analytical expression for the terminal velocity that might be useful for studying regimes of high compression and help in the benchmarking of hydrocodes as well as helping develop nonlinear models in regimes of high compression. This work is structured as follows: in § 2 the one-dimensional background (zero-order) profiles upon which the instability evolves are presented, calculating first the reflected and transmitted shock intensity parameters (z_r, and z_t, respectively). All the background quantities necessary for later calculations are shown as functions of z_r, z_t. The linear theory perturbation problem is presented in § 3. The linearised equations of motion are shown in § 4. The necessity and usefulness of the

https://doi.org/10.1017/jfm.2025.10740 Published online by Cambridge University Press

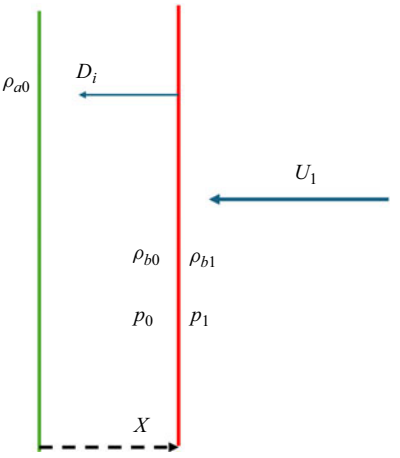


Figure 1. Incident shock and contact surface, before shock refraction at $t = 0$, in one-dimensional geometry. U_1 is the fluid velocity behind the incident shock.

Laplace transform is briefly discussed in § 5. The linearised Rankine Hugoniot equations are shown in § 6. The important functional equations satisfied by the reflected and transmitted shock pressure perturbations are derived in § 7, after discussing the feasibility of a rigid piston approximation (RPA for short). These equations are solved exactly in § 8 using elementary tools of complex calculus in one variable. In § 9, the important method of inverting the Laplace transforms in order to get the temporal evolution of the perturbations is discussed, and explicit analytical formulas are given. The ordinary differential equations satisfied by the components of the asymptotic velocity field are also derived in § 9. The important (1.3) is rederived for easy of discussion.

Let us concentrate on figure 1. An incident shock comes from the right, inside fluid 'b' with velocity $-D_i\hat{x}$ in the laboratory reference frame. The contact surface is initially at rest, and located at $x = 0$. The incident shock hits the contact surface at $t = 0$. Each fluid is assumed to be an ideal gas with specific heat ratios γ_a and γ_b, respectively. The densities of each fluid, before shock compression, are given by ρ_{a0} and ρ_{b0}, respectively. We define here the pre-shock density ratio $R_0 = \rho_{a0}/\rho_{b0}$; see figure 1. We define, following Whitham (Whitham 1973), the incident shock strength parameter $z_i = p_1/p_0 - 1$, with p_0 the initial pressure in both fluids and p_1 the pressure behind the incident shock. If we define the quantity $\epsilon_{b1} = \gamma_b + 1/2\gamma_b$, the upstream incident shock Mach number is equal to

$$M_i = \frac{D_i}{c_{b0}} = \sqrt{1 + \epsilon_{b1} z_i}. \tag{1.1}$$

The quantity c_{b0} is the initial sound speed of fluid 'b' given by

$$c_{b0} = \sqrt{\frac{\gamma_b\ p_0}{\rho_{b0}}}. \tag{1.2}$$

The fluid compressed by the incident shock acquires a velocity $-U_1\hat{x}$ in the laboratory frame of reference and its density increases from ρ_{b0} to ρ_{b1}. The sound speed of the compressed fluid 'b' across the incident shock is indicated with c_{b1}. After shock refraction, on the side of fluid 'a', a transmitted shock propagates to the left with speed D_t The pressure behind the transmitted front is p_f (the same as the pressure in the space between the reflected shock wave and the contact surface) and the corresponding shock strength is $z_t = (p_f - p_0)/p_0$. The transmitted shock Mach number is thus: $M_t = D_t/c_{a0} =$

https://doi.org/10.1017/jfm.2025.10740 Published online by Cambridge University Press

$\sqrt{1+\epsilon_{a1}z_t}$, where $\epsilon_{a1}=\gamma_a+1/2\gamma_a$. After shock compression, the contact surface acquires a normal velocity, which we indicate with U. It is equal to $U=c_{a0}z_t/(\gamma_a M_t)$. We assume a sinusoidal corrugation for the contact surface ripple of the form $\psi_0\cos ky$, where λ is the corrugation wavelength and $k=2\pi/\lambda$ is the perturbation wavenumber, and impose the condition: $\psi_0\ll\lambda$ so that a linear theory analysis is warranted. The incident shock refracts in a time scale of the order of $\Delta t_0\approx 2\psi_0/D_i$, which is therefore very small. For notational simplicity, we indicate this time as $t=0+$. Then, at $t=0+$ a reflected shock or a rarefaction fan are formed inside fluid 'b' and a transmitted shock front is always driven into fluid 'a'. Whether a shock or a rarefaction is formed inside fluid 'b' depends on the incident shock Mach number, the pre-shock density ratio $R_0=\rho_{a0}/\rho_{b0}$ and the isentropic exponents γ_a, and γ_b (Yang *et al.* 1994; Velikovich 1996). In this work we only consider cases in which a shock is reflected. In figure 1 we show a transmitted and reflected shock. If $\gamma_a=\gamma_b$, a shock is reflected if and only if $R_0=\rho_{a0}/\rho_{b0}>1$. If $R_0<1$, a rarefaction will be reflected. However, if $\gamma_a\neq\gamma_b$, the type of front reflected inside fluid 'b' would also be dependent on the incident shock strength, as discussed in Yang *et al.* (1994), Velikovich (1996). In any case, the final density of fluid 'b' at the contact surface is indicated here by ρ_{bf}, its sound speed by c_{bf} and the pressure on side 'b', at the contact surface ($x=0$), is p_f. The final density ratio at the surface is indicated: $R=\rho_{af}/\rho_{bf}$. It is clear that the final pressure of fluid a between the transmitted shock and the contact surface is also p_f.

After $t=0+$, when both fronts have moved one or several perturbation wavelengths away from $x=0$, the normal perturbation velocity at the surface ripple would have almost reached its asymptotic value, which we call δv_{xc}^{∞} (subscript c stands for contact surface). As discussed in Wouchuk (2001*a*, 2001*b*), Wouchuk & Nishihara (1997) and Wouchuk (2025), the asymptotic normal velocity δv_{xc}^{∞} at the contact surface ripple is given by the following exact expression, valid for any shock intensity, in linear theory:

$$\delta v_{xc}^{\infty}=\frac{\delta v_{yb}^{0}-R\delta v_{ya}^{0}}{1+R}+\frac{-\mathcal{F}_b+R\mathcal{F}_a}{R+1}, \tag{1.3}$$

where δv_{ya}^{0} and δv_{yb}^{0} are the values of the tangential velocities generated on each side of the contact surface at $t=0+$ by the corrugated shocks. The quantities $\mathcal{F}_a$ and $\mathcal{F}_b$ are particular averages of the pressure perturbations at the corrugated shock fronts inside both fluids. The term $\mathcal{F}_a$ is proportional to a temporal average of the transmitted shock pressure perturbations in time (Wouchuk & Nishihara 1997; Wouchuk 2001*a*, 2001*b*)

$$\mathcal{F}_a\propto\int_{0+}^{\infty}\delta p_t(t)e^{-\beta_t t}\mathrm{d}t. \tag{1.4}$$

The proportionality constant will be derived later to calculate the velocity profiles inside each fluid. In (1.4) above, the quantity δp_t is the pressure perturbation just behind the transmitted shock front and $\beta_t=(D_t-U)/c_{af}$ is the transmitted shock Mach number with respect to the compressed fluid a. It will be seen that $\mathcal{F}_a$ is negligible for weak shocks (typically, for $M_t\ll 1.5$) but not so for stronger shocks. It is recalled here that $\mathcal{F}_a$ can also be interpreted as a weighted spatial average of the vorticity generated by the transmitted front inside fluid a, see, for example, Wouchuk (2001*a*, 2001*b*), Wouchuk & Nishihara (1997) and Wouchuk (2025). Similarly with $\mathcal{F}_b$.

2. Zero-order profiles

First, it is convenient to develop the equations that give us the zero-order quantities and hence describe the background upon which the instability evolves. Referring to figure 1,

https://doi.org/10.1017/jfm.2025.10740 Published online by Cambridge University Press

we consider an incident shock coming from the right, inside fluid b, with speed D_i in the laboratory frame that hits the contact surface located at $x = 0$, at the instant of time $t = 0$. The pre-shock density of fluid a is ρ_{a0}, and we define the pre-shock density ratio at the contact discontinuity: $R_0 = \rho_{a0}/\rho_{b0}$. Following Yang *et al.* (1994) we define another intensity parameter s for the incident shock

$$s = (p_1 - p_0)/p_1. \tag{2.1}$$

However, it is also convenient for us to work with the intensity parameter z_i, as defined in Whitham's book (Whitham 1973)

$$z_i = (p_1 - p_0)/p_0 = s/(1 - s). \tag{2.2}$$

It is relatively easy to express the different quantities behind the incident shock in terms of z_i, but we use s when comparing with Yang *et al.* (1994).

For later use, it will be necessary to have weak shock expansions of the different zero-order quantities up to order z_i^3, We apologise here that, because of space limitations, we cannot show here all the coefficients appearing in the weak shock third-order expansions, and they should be worked out by the interested reader. Because of this constraint, we show, nevertheless, all the expansion coefficients in the Supplementary materials are available at https://doi.org/10.1017/jfm.2025.10740. It is a Mathematica file, and anyone with some experience using Mathematica should be able to work with it. It is advised, however, that the interested reader takes a look at Supplementary materials, before working with the Mathematica files. The author tried to follow the notation of this paper inside the Mathematica files. We proceed here with the incident shock Mach number expansion

$$M_{inc} \sim 1 + m_{i1} z_i + m_{i2} z_i^2 + m_{i3} z_i^3, \tag{2.3}$$

where its coefficients are easy to obtain

$$m_{i1} = \epsilon_{b1}/2. \tag{2.4}$$

Coefficients m_{i2}, m_{i3} may be found inside Supplementary materials. The incident shock sets fluid b in motion, with velocity $-U_1\hat{x}$, in the laboratory frame. The fluid velocity U_1 is given by

$$\frac{U_1}{c_{b0}} = \frac{z_i}{\gamma_b M_i}. \tag{2.5}$$

The density compression ratio across the incident shock is

$$R_i = \frac{1 + \epsilon_{b1} z_i}{1 + \epsilon_{b2} z_i}, \tag{2.6}$$

where we recall $\epsilon_{b1} = \gamma_b + 1/2\gamma_b$, $\epsilon_{b2} = \gamma_b - 1/2\gamma_b$. The sound speed inside fluid b increases from c_{b0} to c_{b1}, across the incident shock, according to

$$\frac{c_{b1}}{c_{b0}} = \sqrt{\frac{1 + z_i}{R_i}}. \tag{2.7}$$

We rename, for simplicity: $c_{b10} = c_{b1}/c_{b0}$.

The weak shock expansion of c_{b10}can be found inside Supplementary materials.

The downstream shock Mach number of the incident front is

$$\beta_i = \sqrt{\frac{1 + \epsilon_{b2} z_i}{1 + \epsilon_{b1} z_i}} < 1. \tag{2.8}$$

https://doi.org/10.1017/jfm.2025.10740 Published online by Cambridge University Press

At $t = 0$, the incident shock hits the contact surface: a reflected shock goes back inside fluid b and a transmitted shock moves inside fluid a. The pressure in the space between the reflected and transmitted shocks is denoted by p_f. Hence, the reflected and transmitted intensity parameters are (see figure 1)

$$\begin{aligned} z_r &= \frac{p_f - p_1}{p_1}, \\ z_t &= \frac{p_f - p_0}{p_0} \end{aligned} \tag{2.9}$$

Fluid a between the contact surface and the transmitted shock moves to the left with speed U, given by

$$\frac{U}{c_{a0}} = \frac{z_t}{\gamma_a M_t}. \tag{2.10}$$

In units of the incident shock speed, it is equal to

$$\frac{U}{D_i} = \frac{z_t}{\theta\ \gamma_a M_t M_i}, \tag{2.11}$$

where the dimensionless quantity θ above is defined as

$$\theta = \frac{c_{b0}}{c_{a0}} = \sqrt{\frac{\gamma_b R_0}{\gamma_a}}. \tag{2.12}$$

It is noticed that the parameter θ is equal to the reciprocal of Fraley's parameter y (Fraley 1986).

Besides, M_t is the upstream transmitted shock Mach number

$$M_t = \frac{D_t}{c_{a0}} = \sqrt{1 + \epsilon_{a1} z_t} > 1. \tag{2.13}$$

The upstream reflected shock Mach number is

$$M_r = \frac{D_r}{c_{b1}} = \sqrt{1 + \epsilon_{b1} z_r} > 1. \tag{2.14}$$

As will be discussed later, we will need expansions of the background quantities up to order z_i^3 when analysing the weak shock behaviour of the asymptotic velocity. These expansions are shown in detail inside Supplementary materials.

According to figure 1, fluid b between the contact surface and the reflected shock moves to the left with the same speed $-U\hat{x}$ as the contact surface. The downstream Mach number of the transmitted shock, β_t, is given by

$$\beta_t = \frac{D_t - U}{c_{af}} = \sqrt{\frac{1 + \epsilon_{a2} z_t}{1 + \epsilon_{a1} z_t}} < 1. \tag{2.15}$$

Where have defined $\epsilon_{a1} = \gamma_a + 1/2\gamma_a$, and $\epsilon_{a2} = \gamma_a - 1/2\gamma_a$. Correspondingly, the downstream Mach number of the reflected shock is

$$\beta_r = \frac{D_r + U}{c_{bf}} = \sqrt{\frac{1 + \epsilon_{b2} z_r}{1 + \epsilon_{b1} z_r}} < 1. \tag{2.16}$$

It is necessary to define here, for later use, the quantity χ_r

$$\tanh \chi_r = \beta_r\ > 0. \tag{2.17}$$

https://doi.org/10.1017/jfm.2025.10740 Published online by Cambridge University Press

We also define a similar quantity associated with the transmitted shock, called χ_t

$$\tanh \chi_t = -\beta_t < 0. \tag{2.18}$$

The quantity χ_t is negative for reasons that will become clear later on when we solve the linear perturbation problem. We calculate next the density ratios across the reflected and transmitted shocks, respectively,

$$R_{refl} = \frac{1+\epsilon_{b1} z_r}{1+\epsilon_{b2} z_r} > 1, \tag{2.19}$$

$$R_{tr} = \frac{1+\epsilon_{a1} z_t}{1+\epsilon_{a2} z_t} > 1. \tag{2.20}$$

From these values we easily get the ratio of sound velocities across of the reflected and transmitted shock, respectively,

$$\frac{c_{bf}}{c_{b1}} = \sqrt{\frac{1+z_r}{R_{refl}}}, \tag{2.21}$$

$$\frac{c_{af}}{c_{a0}} = \sqrt{\frac{1+z_t}{R_{tr}}}. \tag{2.22}$$

The final density ratio at the contact surface is thus

$$R = R_0/(R_i R_{refl}). \tag{2.23}$$

It is also convenient to have the ratio of post-shock sound velocities at both sides of the contact surface

$$Q = \frac{c_{af}}{c_{bf}} = \frac{c_{af}}{c_{a0}} \frac{c_{b1}}{c_{bf}} \frac{c_{b0}}{c_{b1}} Q_0, \tag{2.24}$$

where Q_0 is its pre-shock value, given by

$$Q_0 = \frac{c_{a0}}{c_{b0}} = \frac{\gamma_a}{\gamma_b}\theta, \tag{2.25}$$

with $\theta = \sqrt{\gamma_b R_0/\gamma_a}$. The quantity θ was defined previously, and is equal to the reciprocal of the quantity y used by Fraley (1986). The quantity Q above is the ratio of post-shock sound speeds at both sides of the contact surface. In our previously published work, we indicated this quantity with the capital letter $\mathcal{N}$, but N is a protected symbol inside Mathematica, and because of this, the letter Q is used inside the Mathematica files appended to this article, namely, inside Supplementary materials.

It is clear that to solve for the background quantities of the zero-order problem we need the shock intensities z_r, z_t as functions of R_0, γ_a, γ_b, z_i.

To this end, the necessary equations result from asking for continuity of pressure and normal velocity at the contact surface. Translated into the language of the variables z_r, z_t, these conditions read

$$z_t = z_i + (1+z_i) z_r, \tag{2.26}$$

$$\frac{z_i}{M_i} - \frac{c_{b1}}{c_{b0}} \frac{z_r}{M_r} = \theta \frac{z_t}{M_t}, \tag{2.27}$$

where $\theta = (\gamma_b/\gamma_a)(c_{a0}/c_{b0})$.

It is very difficult to obtain an explicit analytical solution for z_r, z_t from the above system of equations. However, scientific software like Mathematica usually gives very accurate estimates of z_r, z_t.

https://doi.org/10.1017/jfm.2025.10740 Published online by Cambridge University Press

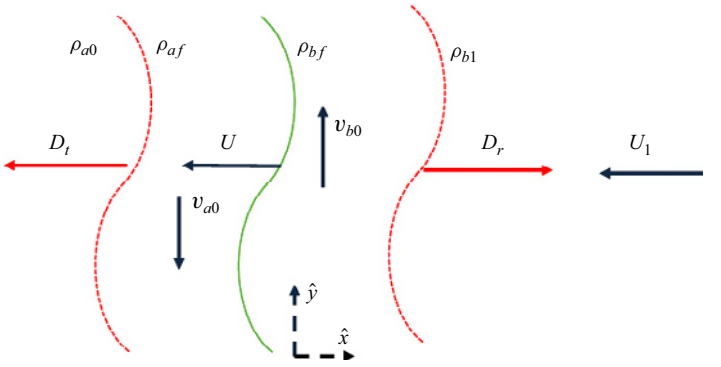


Figure 2. Initial tangential velocities at both sides of the contact surface, after shock refraction at $t = 0+$; two-dimensional geometry.

For later use, we will need the weak shock scaling of the quantities $e^{\pm\chi_r}$, $e^{\pm\chi_t}$. We start with $e^{-\chi_r}$: from (2.17), we easily get

$$e^{-\chi_r} = \sqrt{\frac{1-\beta_r}{1+\beta_r}}. \tag{2.28}$$

If we expand z_r and β_r in powers of z_i, for $z_i \ll 1$ we soon arrive at the lowest possible order in z_i

$$e^{+\chi_r} \sim \frac{1}{\sqrt{z_i}}, \tag{2.29}$$

$$e^{-\chi_r} \sim \sqrt{z_i}. \tag{2.30}$$

Similar scalings hold for $e^{\pm\chi_t}$.

3. Linear perturbation theory

In this section we start considering the situation in which the incident shock hits a corrugated contact surface. We assume an initial corrugation imprinted on the contact surface which depends on the tangential coordinate y in the form: $\psi_c(t=0, y) = \psi_0 \cos ky$, where $k = 2\pi/\lambda$ is the corrugation wavenumber. The corrugation wavelength λ is much larger than the initial ripple amplitude: $\psi_0 \ll \lambda$ so as to ensure the validity of a linear theory. In figure 2 we show the typical geometry after the incident shock refraction ($t = 0+$). Because the contact surface is rippled, the reflected and transmitted wavefronts will be as well. Let $\psi_r(t)\cos ky$ and $\psi_t(t)\cos ky$ be the reflected and transmitted ripple amplitudes, respectively. As is well known, both amplitudes oscillate in a damped fashion, while the shocks separate away from the contact surface. At the same time, pressure perturbations irradiated by the corrugated shocks arrive at the contact surface, get refracted there and continue to catch the shock on the other side of the contact surface. It is noticed here that, because the shocks move with respect to the contact surface, the Doppler effect will be an important mechanism governing the dynamics of the acoustic pressure field. The Doppler effect will have a profound influence in the algebra of the pressure perturbation fields. Since the works of Richtmyer (1960) and Meshkov (1969), it is known that the amplitude of the contact surface ripple reaches a constant velocity of growth (the terminal velocity) when $t \to \infty$, that is, when the refracted shocks are very far from the contact surface (equivalently, for values of the time t such that: $(D_r + U)t \gg \lambda$, $(D_t - U)\, t \gg \lambda$).

https://doi.org/10.1017/jfm.2025.10740 Published online by Cambridge University Press

Before proceeding to solve the fluid equations in the space between the reflected and transmitted shock, it is convenient to briefly discuss here the origin of the fluid perturbations in both fluids. As is well known (Landau & Lifshitz 1986), across the surface of a shock wave, tangential velocity is conserved, and it is this mechanism that lies at the heart of the pressure and velocity perturbation fields' evolution in both fluids, as will become evident later.

Even though the incident shock is planar for $t < 0$, the reflected and transmitted fronts are not, they are corrugated and the initial amplitudes of their ripples are given below.

The initial amplitude of the ripple at the transmitted front is (Richtmyer 1960)

$$\psi_{t0} = \left(1 - \frac{D_t}{D_i}\right) \psi_0, \tag{3.1}$$

and the initial amplitude of the reflected shock ripple is

$$\psi_{r0} = \left(1 + \frac{D_r}{D_i}\right) \psi_0. \tag{3.2}$$

As commented before, the tangential velocity is conserved across each rippled front (Landau & Lifshitz 1986) This fact allows us to calculate the dimensionless velocities v_{a0} and v_{b0} The tangential velocity behind the reflected and transmitted front are, respectively, $\delta v_{yb0} = (U_1 - U)k\ \psi_{r0}$, $\delta v_{ya0} = -Uk \quad \psi_{t0}$ Below, we express both velocities in units of D_i

$$v_{b0} = \frac{\delta_{vyb0}}{D_i} = \left(\frac{U_1}{D_i} - \frac{U}{D_i}\right) k\ \psi_{r0}, \tag{3.3}$$

$$v_{a0} = \frac{\delta v_{ya0}}{D_i} = -\frac{U}{D_i} k\ \psi_{t0}. \tag{3.4}$$

Once the corrugated reflected and transmitted shocks start moving inside their respective fluids, the ripple amplitudes start oscillating and decay in a somewhat damped fashion. This process generates pressure fluctuations behind each front that fill the space in between. These pressure perturbations are responsible of accelerating the fluid particles and hence are responsible of the asymptotic motion of the ripple at the contact surface. Besides, as we will see below, the conservation of tangential velocity at each corrugated front is also responsible of creating vorticity in the compressed fluids. As will be clear later on, the calculation of the vorticity field stored in each fluid is necessary in order to determine the value of the terminal velocity. The weak shock expansions of R, and $v_{a0},\ v_{b0}$ are shown inside Supplementary materials.

4. Linearised fluid equations

We start defining the dimensionless quantities of interest in our work. We recall that we work in a system of reference that moves with velocity U, the velocity of compressed fluid a. First, in order to compare with the results of Yang *et al.* (1994), we express all the perturbation velocities in units of the incident shock speed. Besides, given that we are solving a linear theory problem, all the perturbed quantities of interest are proportional to $k\psi_0$. Hence, we adopt the definitions that follow below. The pressure perturbations inside fluid m are normalised in units of $\rho_{mf} c_{mf} D_i\ k\psi_0$

https://doi.org/10.1017/jfm.2025.10740 Published online by Cambridge University Press

$$\delta v_x(x,\,y,\,t) = u(x,\,t)\;D_i\,\cos ky\;k\psi_0,$$
$$\delta v_y(x,\,y,\,t) = v(x,\,t)\;D_i\,\sin ky\;k\psi_0,$$
$$\delta p_m(x,\,y,\,t) = \rho_{mf}c_{mf}\;D_i\;\hat{p}_m(x,\,t)\cos ky\;k\psi_0, \tag{4.1}$$
$$\delta\rho_m = \rho_{mf}\hat{\rho}_m k\psi_0. \tag{4.2}$$

We consider inviscid, ideal gases. The linearised, non-dimensional equations of motion inside fluid $m = a,\,b$ (we define the dimensionless time ($\tau_m = kc_{mf}t$), are

$$\frac{\partial u_m(x,\,\tau_m)}{\partial\tau_m} = -\frac{\partial\hat{p}_m}{\partial kx},$$
$$\frac{\partial v_m}{\partial\tau_m} = \hat{p}_m, \tag{4.3}$$
$$\frac{\partial\hat{p}_m}{\partial\tau} = \frac{\partial\hat{\rho}_m}{\partial\tau}.$$

The previous equations correspond to the conservation of longitudinal and tangential momentum and energy, respectively. The energy conservation for inviscid fluids is equivalent to the conservation of entropy of the fluid particles (Landau & Lifshitz 1986). As has been extensively used in previous works, it is convenient to change to the variables $r,\,\chi$, inside each fluid, defined by Briscoe & Kovitz (1968) and Zaidel (1960) as

$$kx = r\,\sinh\chi, \tag{4.4}$$
$$\tau_m = r\,\cosh\chi. \tag{4.5}$$

It is easy to see that, inside fluid b, the compressed fluid occupies the region between $\chi = 0$ and $\chi = \chi_r = \tanh^{-1}\beta_r$. The transmitted shock, on the other hand, moves inside fluid a with negative velocity, and hence, compressed fluid a occupies the region between $\chi = \chi_t = -\tanh^{-1}\beta_t$ and $\chi = 0$. This is why χ_t has been defined as a negative quantity in (2.18). Unless strictly necessary, we will not append the subscript m to r or χ. The previously linearised fluid equations can be combined to get the usual sound wave equation inside fluid m

$$\frac{\partial^2\hat{p}_m}{\partial\tau^2} = \frac{\partial^2\hat{p}_m}{\partial(kx)^2} - \hat{p}_m. \tag{4.6}$$

The above equation is a particular form of the Klein–Gordon equation (Morse & Feshbach 1953). For later use, it is convenient to write here the transformation rules between Cartesian coordinates $x,\,t$ and hyperbolic coordinates $r,\,\chi$. The subscript m is omitted for simplicity

$$\frac{\partial}{\partial\tau} = \cosh\chi\,\frac{\partial}{\partial r} - \frac{\sinh\chi}{r}\,\frac{\partial}{\partial\chi}, \tag{4.7}$$
$$\frac{\partial}{\partial kx} = -\sinh\chi\,\frac{\partial}{\partial r} + \frac{\cosh\chi}{r}\,\frac{\partial}{\partial\chi}, \tag{4.8}$$

Equation (4.6) is easily solved within the domain of the variables $(r,\,\chi)$, as has been done in Wouchuk & Nishihara (1996, 1997). After the corresponding algebra, we get, see Wouchuk (2001*a*, 2025),

$$r\frac{\partial^2\hat{p}_m}{\partial r^2} + \frac{\partial\hat{p}_m}{\partial r} + r\,\hat{p}_m = \frac{\partial\hat{j}_m}{\partial\chi}, \tag{4.9}$$

https://doi.org/10.1017/jfm.2025.10740 Published online by Cambridge University Press

where

$$j_m = \frac{1}{r}\frac{\partial \hat{p}_m}{\partial \chi}. \tag{4.10}$$

We recall here that $-j(\chi = 0, r)$ is equal to the fluid perturbed normal acceleration at $x = 0$. As has been previously shown in Briscoe & Kovitz (1968) and Wouchuk & Nishihara (1996), the wave equation above can be always solved by separation of variables, and inside each fluid, we can write the solution as

$$\hat{p}_m(\chi, r) = \sum_{\nu=1}^{\infty} D_{m\nu}(\chi) J_\nu(r), \tag{4.11}$$

where J_ν is the ordinary Bessel function of order ν, and

$$D_{m\nu}(\chi) = \pi_{m\nu} \cosh \nu\chi + \omega_{m\chi} \sinh \nu\chi. \tag{4.12}$$

Coefficients $\pi_{m\nu}, \omega_{m\nu}$ have to be calculated from the boundary conditions at both shocks and the contact surface, as in Wouchuk & Nishihara (1996). The convergence of the series given by (4.12) has been recently proved in Wouchuk (2025). The function j_m is also written as a Bessel series of the form

$$j_m(\chi, r) = \sum_{\nu=1}^{\infty} E_\nu(\chi) \frac{\nu J_\nu(r)}{r}, \tag{4.13}$$

with

$$E_\nu(\chi) = \pi_{m\nu} \sinh \nu\chi \ + \omega_{m\nu} \cosh \nu\chi. \tag{4.14}$$

The coefficients $\pi_{m\nu}, \omega_{m\nu}$ can be calculated according to the procedure explained in Wouchuk & Nishihara (1996), in order to avoid round-off errors. The interested reader can calculate them using Supplementary materials.

5. Method of solution using Laplace transforms

It has proved very useful to solve the wave equation (4.10) by means of the Laplace transform; see Wouchuk & Nishihara (1996, 1997) and Wouchuk (2001*a*, 2025). The main motivation behind this method lies in two important facts:

(i) Solving for the Laplace transform of the shock pressure perturbation at each corrugated shock, allows us, after a standard inverse transformation, to follow the temporal evolution of those perturbations for large times, something that is very difficult to do with Bessel series because of the accumulation of round-off errors.

(ii) Besides, once we have an analytical expression for the Laplace transforms, all the quantities of interest, like the terminal velocity of the ripple at the contact surface, can be obtained as an *a priori* explicit analytic function of the parameters that govern the problem: fluid compressibilities, pre-shock density ratio and incident shock Mach number. This method has been pioneered by G. Fraley as early as 1986 in Fraley (1986).

We set the notation in what follows. For any function $\phi(\chi, r)$, we define its Laplace transform as (indicating it with capital letters)

$$\Phi(\chi, s) = \int_0^\infty \phi(\chi, r) e^{-s\,r}\, \mathrm{d}r. \tag{5.1}$$

https://doi.org/10.1017/jfm.2025.10740 Published online by Cambridge University Press

If we simultaneously take the Laplace transform of (4.10) and (4.11), and make: $s = \sinh q$, we get the system of equations (Wouchuk 2001*a*)

$$\frac{\partial}{\partial q}\left[\cosh q\, P(\chi, q)\right] + \frac{\partial J(\chi, q)}{\partial \chi} = 0, \tag{5.2}$$

$$\frac{\partial J(\chi, q)}{\partial q} + \frac{\partial}{\partial \chi}\left(\cosh q\, P(\chi, q)\right) = 0. \tag{5.3}$$

The above system can be easily integrated by changing to the variables $q + \chi$, $q - \chi$, and we get a system of first integrals

$$J_m(\chi, q + \chi)\cosh(q + \chi) P_m(\chi, q + \chi) = 2F_{m1}(q), \tag{5.4}$$

$$-J_m(\chi, q - \chi) + \cosh(q - \chi) P_m(q - \chi) = 2F_{m2}(q), \tag{5.5}$$

where $m = a, b$ depending on which side of the contact surface we are considering the perturbation field. The functions $F_{m1,2}$ must be determined by applying the boundary and initial conditions. First, we easily see that P_m, J_m can be recast in the form

$$P_m(\chi, q) = \frac{F_{m1}(q - \chi) + F_{m2}(q + \chi)}{\cosh q}, \tag{5.6}$$

$$J_m(\chi, q) = F_{m1}(q - \chi) - F_{m2}(q + \chi). \tag{5.7}$$

If we take the Laplace transform of the function defined in (4.12) (after using the fact that the Laplace transform of the Bessel function $J_\nu(r)$ is $e^{-\nu q}/\cosh q$, and that of $\nu\, J_\nu(r)/r$ is: $e^{-\nu q}$), we can identify

$$F_{m1}(q) = \sum_{\nu=1}^{\infty} s_{m\nu} e^{-\nu q}, \tag{5.8}$$

$$F_{m2}(q) = \sum_{\nu=1}^{\infty} d_{m\nu}, e^{-\nu q}\ , \tag{5.9}$$

where $s_{m\nu}$, $d_{m\nu}$ are defined immediately below. The Laplace transform of (4.12) is

$$P_m(q_m) = \sum_{\nu=1}^{\infty} D_{m\nu} \frac{e^{-\nu q}}{\cosh q}. \tag{5.10}$$

The coefficients $s_{m\nu}$, $d_{m\nu}$ are

$$\begin{aligned} s_{m\nu} &= \frac{\pi_{m\nu} + \omega_{m\nu}}{2}, \\ d_{m\nu} &= \frac{\pi_{m\nu} - \omega_{m\nu}}{2}. \end{aligned} \tag{5.11}$$

We recall that the details on how to derive the coefficients π_ν^m, ω_ν^m avoiding round-off errors can be found in Wouchuk & Nishihara (1996). Besides, the interested reader may always use Supplementary materials.

We recall that $-j_m(\chi = 0, \tau_m)$ is equal to the fluid normal acceleration at the contact surface ripple on the side of fluid m. It is very important, for later use, to show here the behaviour of its Laplace transform $J_{mc}(q_m)$ as a function of q_m; subscript c means contact surface throughout this work. $J_{bc}(q_b) = J_{ac}(q_a)$, where q_a and q_b are related by $Q\ \sinh q_a = \sinh q_b$, in which $Q = c_{af}/c_{bf}$. Because of continuity of the normal velocity, we call this function $J_c(q)$ for simplicity. In figure 4 we show $|J_c(q_b)|$ for the gas and shock

https://doi.org/10.1017/jfm.2025.10740 Published online by Cambridge University Press

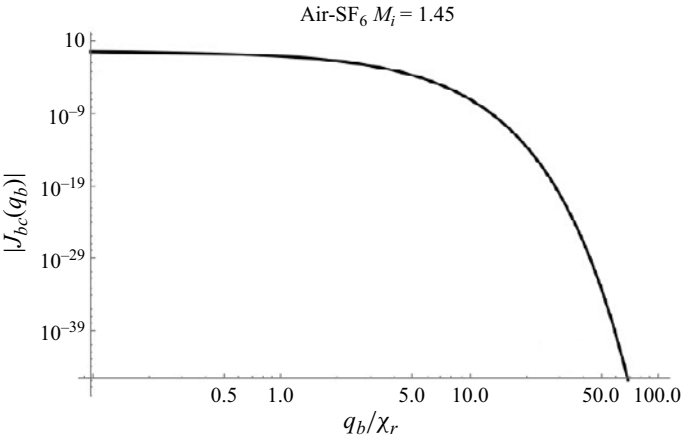


Figure 3. Behaviour of $|J_c(q_b)|$ as a function of q_b for the parameters indicated.

parameters indicated, evaluated with coefficients $\omega_{b\nu}$ inside (5.13), because the simplest way of evaluating J_c is using the infinite series

$$J_c(q_b) = \sum_{\nu=1}^{\infty} \omega_{b\nu} \ \ e^{-\nu q_b}. \tag{5.12}$$

Later on, we will derive an explicit analytic expression for $J_c(q_b)$. It is convenient that we plot $J_c(q_b)$. This is shown in figure 3. The plot in figure 3 was computed with 51 terms inside the sum. As for the corresponding function at the reflected shock, it is easy to see that

$$J_r(q_b) = \sum_{\nu=1}^{\infty} E_\nu(\chi_r) e^{-\nu q_b}, \tag{5.13}$$

where the coefficients $E_\nu(\chi_r)$ have been defined in (4.15).

We see, from figure 3, that $J_{bc}(q_b) \sim 0$, for $q_b \geqslant \chi_r$. Similarly inside fluid a: $J_{ac}(q_a) \sim 0$, because of normal velocity continuity at the rippled surface. This fact will allow us later on to get a simplified (albeit approximate) system of functional equations for $P_r(q_b)$ and $P_t(q_a)$, much simpler than equations (65, 66) of Wouchuk (2001*a*). This means that we can approximate: $F_{b1}(q_b) \sim F_{b2}(q_b)$, for $q_b > \chi_r$ and $F_{a1}(q_a) \sim F_{a2}(q_a)$ for $q_a > |\chi_t|$. This behaviour allows us to approximate: $F_{m1}(q_m) \sim F_{m2}(q_m)$. This approximation is called here the RPA, because, for a true rigid piston, as in Wouchuk (2025), the equality between both functions holds exactly: $F_{m1}(q_m) = F_{m2}(q_m)$. The RPA will become very useful later on to construct decoupled functional equations satisfied by the pressure perturbations at both shock fronts.

We proceed next by writing the linearised Rankine Hugoniot equations at each corrugated shock. We recall again that we work in a reference system that comoves with the velocity U of the shocked contact surface.

6. Linearised Rankine Hugoniot equations

The time evolution of the reflected shock ripple amplitude, $\psi_r(\tau)$, is governed by the pressure fluctuations behind the reflected shock, through the equations

$$\frac{\partial \psi_r}{\partial \tau_b} = A_{sr} \psi_0 \hat{p}_r, \tag{6.1}$$

https://doi.org/10.1017/jfm.2025.10740 Published online by Cambridge University Press

$$A_{sr} = \frac{R_{refl}}{R_{refl} - 1} \frac{M_r^2 - 1}{2M_r^2 \beta_r}. \tag{6.2}$$

At any value of the dimensionless time τ_b, conservation of tangential momentum across the reflected shock (Landau & Lifshitz 1986) is responsible of generating the corresponding tangential velocity perturbation behind it

$$v_r(\tau_b) = \frac{U_1 - U}{D_i} \psi_r. \tag{6.3}$$

The density perturbations are related to the pressure perturbations through the equations

$$\begin{aligned} \hat{\rho}_r(r) &= A_{\rho r}\ \hat{p}_r(r), \\ A_{\rho r} &= \frac{1}{2M_r^2\ \beta_r^2}. \end{aligned} \tag{6.4}$$

It is understood that these functions are evaluated just behind the corrugated shock, that is, at $\chi = \chi_r$.

The longitudinal velocity behind the reflected shock is given by

$$\begin{aligned} u_r(r) &= A_{xr}\ \hat{p}_r(r), \\ A_{xr} &= \frac{M_r^2 + 1}{2M_r^2 \beta_r}. \end{aligned} \tag{6.5}$$

Behind the transmitted front we have, similarly

$$\begin{aligned} u_t(r) &= A_{xt}\ \hat{p}_t(r), \\ A_{xt} &= \frac{M_t^2 + 1}{2M_t^2 \beta_t}. \end{aligned} \tag{6.6}$$

The dimensionless tangential velocity behind the reflected shock, in units of the incident shock speed, is

$$v_r(\tau) = \frac{U_1 - U}{D_i} \psi_r(\tau). \tag{6.7}$$

Similarly, the tangential velocity perturbation behind the transmitted front is

$$v_t(\tau) = -\frac{U}{D_i} \psi_t(\tau). \tag{6.8}$$

The time evolution of the transmitted shock ripple amplitude, $\psi_t(\tau)$ satisfies the equations

$$\begin{aligned} \frac{\partial \psi_t}{\partial \tau_a} &= A_{st} \psi_0 \hat{p}_t, \\ A_{st} &= \frac{R_{tr}}{R_{tr} - 1} \frac{M_t^2 - 1}{2M_t^2 \beta_t}. \end{aligned} \tag{6.9}$$

The density perturbations behind the transmitted shock are related to the pressure perturbations through the equations

$$\begin{aligned} \hat{\rho}_t(r) &= A_{\rho t}\ \hat{p}_r(r), \\ A_{\rho t} &= \frac{1}{2M_t^2\ \beta_t^2}. \end{aligned} \tag{6.10}$$

https://doi.org/10.1017/jfm.2025.10740 Published online by Cambridge University Press

To solve the linear perturbation problem we will solve for the Laplace transforms $P_r(q_b)$ and $P_t(q_a)$.

The best strategy is to follow Richtmyer (1960) and take the time derivative of (6.5) and of (6.6) following the reflected and transmitted shocks, respectively. For the reflected shock, we get the relationship (from now on, we use the notation: $\xi_r = k\psi_r$, $\xi_t = k\psi_t$)

$$j_r(r_b) = -A_{xr}\frac{\partial \hat{p}_r}{\partial r} + A_{yr}\beta_r\xi_r, \tag{6.11}$$

where $A_{yr} = (U_1 - U)/D_i$. The subscript r indicates that the function j is evaluated just behind the reflected front, at $\chi = \chi_r$. If we take the Laplace transform of (6.11), we obtain

$$J_r(q_b) = \alpha_{b1}(q_b)\ P_r(q_b) + \alpha_{b2}(q_b), \tag{6.12}$$

which is equivalent to (2.25) of Wouchuk (2025), where

$$\alpha_{b1}(q_b) = \alpha_{b10}\sinh q_b + \frac{\alpha_{b11}}{\sinh q_b}, \tag{6.13}$$

with

$$\alpha_{b10} = -A_{xr}, \tag{6.14}$$

$$\alpha_{b11} = -\frac{1}{2\beta_r}. \tag{6.15}$$

Similarly for the transmitted shock

$$J_t(q_a) = \alpha_{a1}(q_a)\ P_t(q_a) + \alpha_{a2}(q_a), \tag{6.16}$$

with

$$\alpha_{a1}(q_a) = \alpha_{a10}\sinh q_a + \frac{\alpha_{a11}}{\sinh q_a}, \tag{6.17}$$

where

$$\alpha_{a10} = -\frac{M_t^2 + 1}{2M_t^2\beta_t}, \tag{6.18}$$

and

$$\alpha_{a11} = -\frac{1}{2\beta_t}. \tag{6.19}$$

It is convenient that we recall here the behaviour of the functions $J_{ac}(q_a)$ and $J_{bc}(q_b)$ as functions of q_a, q_b, respectively. To this end we must pay attention to figure 3. Please note that, because of normal velocity continuity at the contact surface, this relationship holds: $J_{bc}(q_b) \equiv J_{bc}(q_b) = J_{ac}(q_a) \equiv J_{ac}(q_a)$, where q_a and q_b are related by $Q\sinh q_a = \sinh q_b$. For simplicity, we define $J_c(q_b) = J_{bc}(q_b)$.

In figure 3 we show the function $J_c(q_b)$ for the pre-shock parameters indicated.

Motivated by figure 3, we make the approximations

$$\begin{aligned} J_{ac}(q_a) &\sim 0,\ (q_a \geqslant 1),\\ J_{bc}(q_b) &\sim 0,\ (q_b \geqslant 1). \end{aligned} \tag{6.20}$$

For a truly rigid piston surface, the function J_c is exactly equal to zero (Wouchuk 2001*a*; 2025), therefore, if we make $J_c(q_m) \sim 0$, for a real contact surface, this is only an approximation, which will be called a RPA. It is emphasised here that the RPA embodied in (6.20) constitutes an approximation that may fail if the gases and/or shock Mach are

https://doi.org/10.1017/jfm.2025.10740 Published online by Cambridge University Press

varied and this will have an influence when we calculate the terminal velocity, as it might be a source of error. The error incurred in the calculation of the terminal velocity because of assuming (6.20) will be analysed with detail in § 16 after the results for the terminal velocity are presented.

7. Functional equations satisfied by $P_r(q_b)$ and $P_{t(q_a)}$

Let us briefly recall the relationship between J_r and P_r

$$J_r(q_b) = \alpha_{b1}(q_b) P_r(q_b) + \alpha_{b2}(q_b). \tag{7.1}$$

If in (5.6) we use the above presented approximations ($F_{b1} \sim F_{b2}$, $F_{a1} \sim F_{a2}$), we easily arrive to the following functional equation for $P_r(q_b)$:

$$P_r(q_b) = \lambda_{b1}(q_b) + \lambda_{b2}(q_b) P_r(q_b + 2\chi_r). \tag{7.2}$$

The auxiliary functions are

$$\lambda_{b1}(q_b) = \frac{\alpha_{b2}(q_b) + \alpha_{b2}(q_b + 2\chi_r)}{\cosh q_b - \alpha_{b1}(q_b)}, \tag{7.3}$$

$$\lambda_{b2}(q_b) = \frac{\alpha_{b1}(q_b + 2\chi_r) + \cosh(q_b + 2\chi_r)}{\cosh q_b - \alpha_{b1}(q_b)}. \tag{7.4}$$

We notice here that $\lambda_{b1,2}$ above are exactly the same functions shown in (44) and (45) of Wouchuk (2001*a*), and (36a, 36b) of Wouchuk (2025) which is no surprise, because for a rigid piston, the relationships $F_{b1} = F_{b2}$, $F_{a1} = F_{a2}$, hold exactly.

We proceed in the same manner with the transmitted shock and arrive at a similar functional equation for $P_t(q_a)$

$$P_t(q_a) = \lambda_{a1}(q_a) + \lambda_{a2}(q_a) P_t(q_a - 2\chi_t), \tag{7.5}$$

where

$$\lambda_{a1}(q_a) = -\frac{\alpha_{a2}(q_a) + \alpha_{a2}(q_a - 2\chi_t)}{\cosh q_a + \alpha_{a1}(q_a)}, \tag{7.6}$$

$$\lambda_{a2}(q_a) = \frac{\cosh(q_a - 2\chi_t) - \alpha_{a1}(q_a - 2\chi_t)}{\cosh q_a + \alpha_{a1}(q_a)}. \tag{7.7}$$

We notice here two important facts

$$\begin{aligned} \lambda_{a2}(q_a = 0) &= 0, \\ \lambda_{b2}(q_b = 0) &= 0. \end{aligned} \tag{7.8}$$

It is mentioned here that for ideal gas equation of state (EOS), the denominators of the auxiliary functions ($\lambda_{a1,2}$, $\lambda_{b1,2}$) above never vanish, which means that P_r and P_t do not have poles and hence they are analytic functions of their arguments in the complex plane. Therefore, in such a case, the phenomenon of spontaneous acoustic emission (SAE) is excluded (Wouchuk & Cavada 2004). However, SAE might occur for other EOS, as shown in Wouchuk & Cavada (2004), Calvo-Rivera, Velikovich & Huete (2023) and Napieralski *et al.* (2024) The functional equations presented above are extremely difficult solve exactly and different methods have been tried in the past to extract useful information from them (Wouchuk 2001*a*, 2025). In this work, and thanks to the analyticity of the functions P_r and P_t in the complex plane, we can show the exact solutions of (7.2) and (7.5). We show this solution in the following section.

https://doi.org/10.1017/jfm.2025.10740 Published online by Cambridge University Press

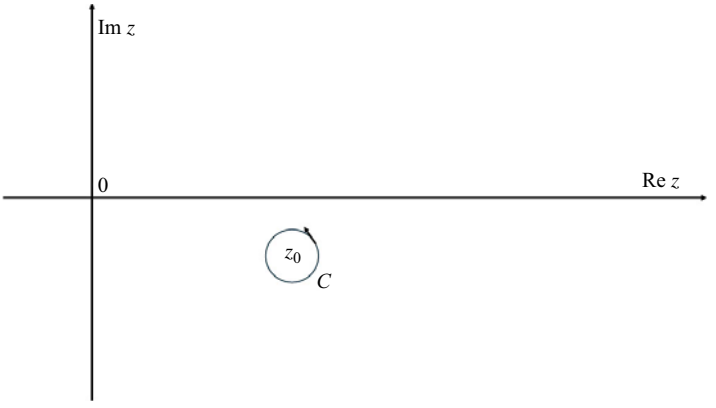


Figure 4. Contour of integration C in the complex plane, used in (8.1).

8. Exact solution of the functional equations (7.2) and (7.5)

We need some concepts from calculus in one complex variable. We refer to the classical textbook of Churchill (1974).

First, we recall the Cauchy integral formula (see page 129 of Churchill 1974). We consider a function f that is analytic everywhere within and on a simple closed contour C oriented counterclockwise. If z_0 is any point interior to C, then, the Cauchy integral formula holds

$$f(z_0) = \frac{1}{2\pi i}\int_C \frac{f(z)}{z - z_0}\mathrm{d}z, \tag{8.1}$$

where i is the imaginary unit.

As discussed before, our functions of interest $P_r(q_b)$, and $P_t(q_a)$ are analytic functions in their corresponding complex planes. Hence, (8.1) can be used with both of them. The idea is straightforward: we divide both members of (7.2) by $2\pi i\ (q_b - q_0)$ where q_0 is an arbitrary complex number, and integrate along a curve C centred at $q = q_0$. We arrive at the equation

$$\frac{1}{2\pi i}\int_C \frac{P_r(q_b)}{q_b - q_0}\mathrm{d}q = \frac{1}{2\pi i}\int_C \frac{\lambda_{b1}(q_b)}{q_b - q_0}\mathrm{d}q_b + \frac{1}{2\pi i}\int_C \frac{\lambda_{b2}(q_b)P_r(q_b + 2\chi_r)}{q - q_0}\mathrm{d}q_b. \tag{8.2}$$

Thanks to the analyticity of P_r, the contour of the last integral in the above equation can be deformed in such a way to make $q_0 = 0$, and hence, the contour C is centred at the origin (but only for the last integral inside (8.2)) Hence, (8.1) can be immediately applied, and recalling that $\lambda_{b2}(q_b = 0) = 0$, we get

$$P_r(q_0) = \lambda_{b1}(q_0). \tag{8.3}$$

As q_0 is an arbitrary complex number in the above equation, we deduce $P_r(q_b) = \lambda_{b1}(q_b)$ for any complex number q_b. Similar arguments hold for the transmitted shock and we deduce

$$P_t(q_a) = \lambda_{a1}(q_a). \tag{8.4}$$

It is very important to notice that the functions $\lambda_{m1,2}(q_m)$ are not independent of each other. They are related because of the Rankine Hugoniot equations, through the auxiliary coefficients $\alpha_{m10}, \alpha_{m11}$. This means that the solution obtained for the above functional equations (7.2, 7.5), may not be generalised to arbitrarily created functional equations.

https://doi.org/10.1017/jfm.2025.10740 Published online by Cambridge University Press

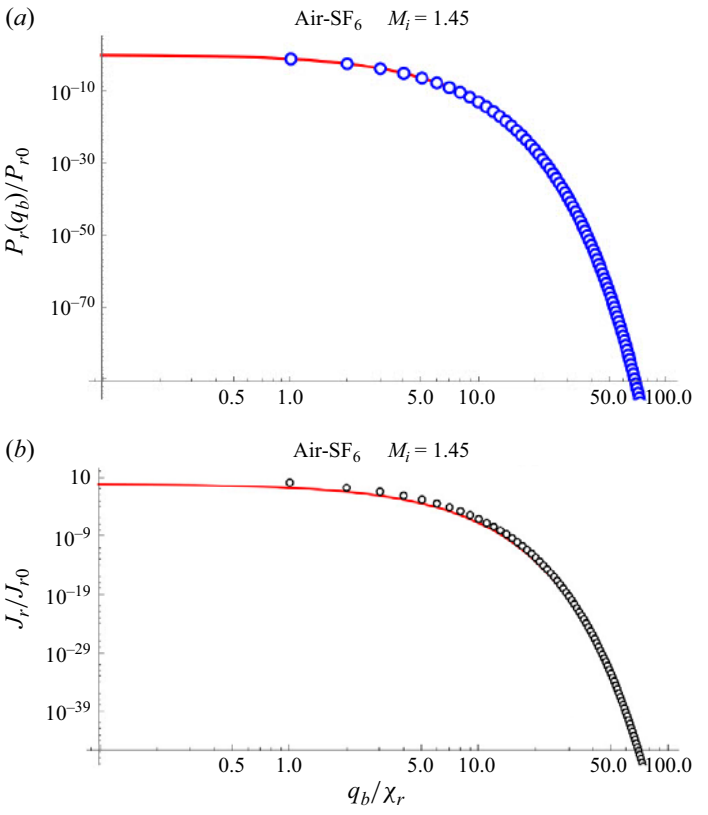


Figure 5. (*a*) Comparison of the function $P_{r1}(q_b)$ defined in (8.11) with the corresponding Bessel series (5.11), for the gases and Mach number indicated. The quantity $P_{r0} = \lim_{q_b \to 0}[\lambda_{b1}(q_b)]$ (*b*) A similar comparison, but for the function $J_r(q_b)$, defined in (6.12) and in (7.1), $J_{r0} = \lim_{q_b \to 0}[J_r(q_b)]$.

Let us consider, for example, the following, totally invented equation, to illustrate with an example:

$$f(x) = \cos x + \sin x \; f(x + \pi/2). \tag{8.5}$$

It is clear that $\cos x$, $\sin x$ are analytic in the whole complex plane, and $\sin 0 = 0$. However, this does not mean that the solution to the above equation is $f(x) = \cos x$ as can be easily verified. Anyway, the method described in § 8, might be of help for other functional equations, with proper modifications, depending on the particular functional equation to be solved. The key point in § 8 has been the analyticity of all the functions appearing in the functional equations. We can compare the solution obtained above for P_r with the solution for $P_r(q_b)$ expressed as a series of decaying exponentials, obtained after solving the corresponding wave equation by separation of variables. This comparison is shown in figure 5(*a*,*b*) for the shock and fluid parameters indicated. Before proceeding to calculate the terminal velocity, it is necessary to pay attention to the following fact: the function $\lambda_{a1}(q_a)$, if evaluated at $q_a = \chi_t$, gives $\lambda_{a1}(\chi_t) = 0$. As a consequence, the flux of the vorticity generated by the transmitted shock, represented by the quantity F_a defined in (9.28), will be identically zero. This absurd result has a tragic consequence: it will lead to an intolerable error in the terminal velocity calculation. If $F_a = 0$ is plugged into (9.28), will give a very poor comparison with the linear simulations of Yang *et al.* (1994). This does not mean that (8.4) is incorrect. The solution found to the functional

https://doi.org/10.1017/jfm.2025.10740 Published online by Cambridge University Press

equations is correct. The problem of getting $F_a = 0$ is because the functional equations themselves are approximate. They have been obtained after approximating $J_{mc}(q_m) \sim 0$ on each side of the contact surface, that is, using the RPA. This problem did not arise in Wouchuk (2001*a*), because the complete boundary conditions at the contact surface had been used in that work. The only way to circumvent this serious nuisance here has been to iterate once on the trial function defined below. That is, in order to calculate the quantity F_a to be plugged in (9.28), we use the iterated function

$$P_{t1}(q_a) = \lambda_{a1}(q_a) + \lambda_{a2}(q_a) P_{ttrial}(q_a - 2\chi_t). \tag{8.6}$$

The function $P_{ttrial}(q_a)$ is built using the RPA. That is, motivated by (43, 44) of Wouchuk (2025) we use

$$P_{ttrial}(q_a) = D_{t1} \frac{e^{-q_a}}{\cosh q_a}, \tag{8.7}$$

where the coefficient D_{t1} is taken from Wouchuk (2025)

$$D_{t1} = \frac{2\alpha_{a20}}{\beta_t - \alpha_{a10} \cosh \chi_t}. \tag{8.8}$$

Later on, we will see that, in order to calculate the temporal evolution of the shock pressure perturbations at the reflected shock, and compare with the Bessel series solution given by (4.12), we will also need to iterate once on a adequately chosen trial function at the reflected shock, in the same way as has been done above for the transmitted shock. We define similarly for the reflected shock

$$P_{rtrial}(q_b) = D_{r1} \frac{e^{-q_b}}{\cosh q_b}, \tag{8.9}$$

where, analogously to D_{t1}, we have

$$D_{r1} = \frac{2\alpha_{b20}}{\beta_r - \alpha_{b10} \cosh \chi_r}. \tag{8.10}$$

Therefore, to calculate the temporal evolution of the reflected shock pressure perturbations, we use the function

$$P_{r1}(q_b) = \lambda_{b1}(q_b) + \lambda_{b2}(q_b) P_{rtrial}(q_b + 2\chi_r). \tag{8.11}$$

With the function $P_{r1}(q_b)$ above, we define $J_{r1}(q_b)$

$$J_{r1}(q_b) = \alpha_{b1}(q_b) P_{r1}(q_b) + \alpha_{b2}(q_b). \tag{8.12}$$

The functions $P_{r1}(q_b)$ and $J_{r1}(q_b)$ are compared with the corresponding Bessel series in figure 5.

Referring to figure 5, we see that the iterated solution $P_{r1}(q_b)$, as given above agrees very well with the solution given by (5.11), and the function $J_{r1}(q_b)$ also agrees neatly with (7.1). For later purposes, when we study the growth of the contact surface ripple, it is necessary to show here the explicit form of the function $J_c(q_b)$ in terms of the solution found above for $P_r(q_b)$. We recall that $J_c(q_b) = F_{b1}(q_b) - F_{b2}(q_b)$. Hence, from (5.6), we get

$$\begin{aligned} J_c(q_b) = {} & J_{r1}(q_b + \chi_r) + J_{r1}(q_b - \chi_r) + \cosh(q_b + \chi_r) P_{r1}(q_b + \chi_r) \\ & - \cosh(q_b - \chi_r) P_{r1}(q_b - \chi_r). \end{aligned} \tag{8.13}$$

The above expression for $J_c(q_b)$ will be necessary later on to analyse the asymptotic contact surface ripple growth in § 15, and also to estimate the relative error in the calculation of the terminal velocity in § 16.

https://doi.org/10.1017/jfm.2025.10740 Published online by Cambridge University Press

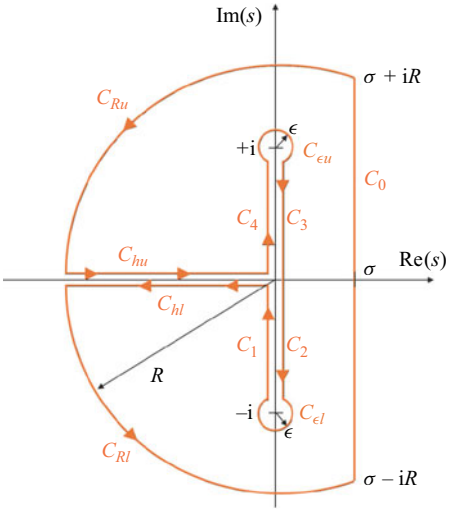


Figure 6. Bromwich contour used to invert the Laplace transforms P_r, P_t.

9. Inverse Laplace transforms

In order to compute $\hat{p}_r(r)$ and $\hat{p}_t(r)$ in the domains of the corresponding variable r, we must invert the functions $P_r(q_b)$ and $P_t(q_a)$ by contour integration in the complex plane. We start with the reflected shock (Zwillinger 1983; Wouchuk 2025).

The integral that corresponds to $\hat{p}_r(r)$ is given by

$$\hat{p}_r(r_b) = \frac{1}{2\pi i}\int_{\mathcal{C}} P_r(s_b) e^{s_b r_b}, \tag{9.1}$$

where the contour of integration C is located to the right of the singularities of P_r, that is, in the semiplane $Res > 0$, and i is the imaginary unit: $i^2 = -1$, as indicated in figure 5. As the procedure to calculate the above integral has been thoroughly detailed recently in Wouchuk (2025), it will not be repeated here. Anyway, those details can also be found on any textbook on the subject like that of Sneddon (1972).

It is worth recalling here that the only singularities exhibited by P_r, P_t are not poles, but branch points at $s_m = \pm i$. The origin of the branch points is the square root term $\sqrt{s^2+1}$ originating from $\cosh q$, which in turn originates from the term $r\ \hat{p}_m(r)$ on the left-hand side of (4.10) that comes from the conservation of tangential momentum. As discussed in Huete *et al.* (2012), these branch points are responsible for the late time decay $p_r(r) \sim r^{-3/2}$ at large times, a behaviour already noticed by Fraley in Fraley (1986). As an important conclusion, we can say that the asymptotic late time decay as $r^{-3/2}$ is caused by the lateral sound waves travelling parallel to shock surfaces (Fraley 1986).

Before calculating the integral of (9.1), we adopt the following conventions: $P_r^+(s)$ corresponds to the value of P_r that results when considering the positive determination of the square roots of the form $\sqrt{s_b^2+1}$ inside $\lambda_{b1}(q_b)$ and $\lambda_{b2}(q_b)$. Analogously, $P_r^-(s)$ is obtained considering the negative determination $-\sqrt{s^2+1}$ of the term $\cosh q_b$ After some algebra, we arrive at

$$\hat{p}_r(r) = \int_{-1}^{+1} f_{rc}(z_b)\cos((z_b r)\ \mathrm{d}z_b, \tag{9.2}$$

https://doi.org/10.1017/jfm.2025.10740 Published online by Cambridge University Press

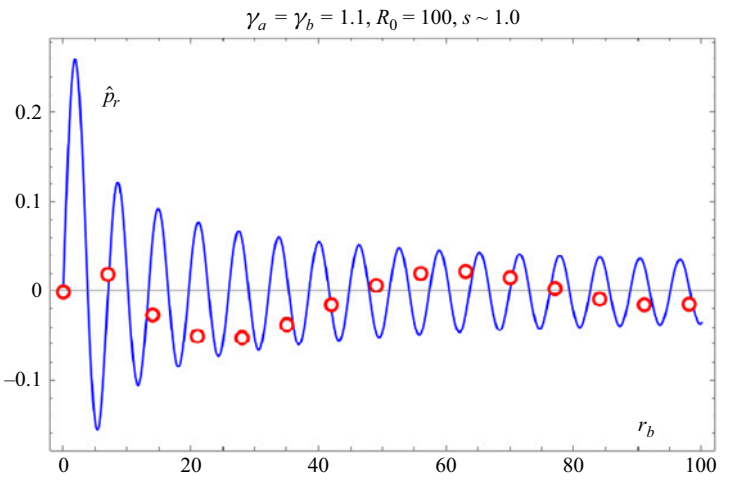


Figure 7. Blue continuous line is the function $\hat{p}_r(r_b)$ obtained after inverting (8.11) in the complex plane for the parameters indicated. Besides, the red, empty circles are calculated with the Bessel series given in (50).

$$+\int_{-1}^{+1} f_{rs}(z_b)\,\sin(z_b r)\,\mathrm{d}z_b, \tag{9.3}$$

with

$$f_{rc}(z_b) = -\frac{1}{2\pi}\mathrm{Re}\,[D_r(z_b)], \tag{9.4}$$

$$f_{rs}(z_b) = \frac{1}{2\pi}\mathrm{Im}\,[D_r(z_b)], \tag{9.5}$$

and $D_r(z_b) = P_r^-(i z_b) - P_r^+(i\ z_b)$. Before proceeding, it is important to mention here the initial condition $\hat{p}_r(r=0)=0$, as discussed by Richtmyer in Richtmyer (1960). It can be seen that $f_{rc}(z)=0$ in (9.5) for any choice of the pre-shock parameters, which, when plugged into (9.3) ensures $\hat{p}_r(r=0)=0$.

In figure 7, we show $p_r(r)$, calculated with (9.3). Similar calculations allow us to write an analogous compact form of $\hat{p}_t(r)$

$$\hat{p}_t(r) = \int_{-1}^{+1} f_{tc}(z_a)\,\cos(z_a r)\mathrm{d}z_a, \tag{9.6}$$

$$+\int_{-1}^{+1} f_{ts}(z_a)\,\sin(z_a r)\,dz_a, \tag{9.7}$$

with

$$f_{tc}(z_a) = -\frac{1}{2\pi}\mathrm{Re}\,[D_t(z_a)], \tag{9.8}$$

$$f_{ts}(z_a) = \frac{1}{2\pi}\mathrm{Im}\,[D_t(z_a)], \tag{9.9}$$

and $D_t(z_a) = P_t^-(i\ z_a) - P_t^+(i\ z_a)$. Similarly to the reflected shock, it can be seen that $f_{tc}(z)=0$.

Referring to figure 7, we mention that it is almost impossible to calculate $p_r(r_b)$, $p_t(r_a)$ for very large times with the series of Bessel functions, because of the accumulation of round-off errors. It is important to notice that the inverse Laplace transformation procedure

https://doi.org/10.1017/jfm.2025.10740 Published online by Cambridge University Press

has been performed on the iterated function $P_{r1}(q_b)$. Inverting only $\lambda_{b1}(q_b)$ gives a poor comparison with the Bessel series solution. The reason is easy to understand: in any RMI problem, there is a strong interaction between the shock fronts and the contact surface, via sonic reverberations. These sonic reverberations are mathematically taken into account in the functional equation for the Laplace transforms inside the shifted arguments of $P_r(q_b + 2\chi_r)$, and $P_t(q_a - 2\chi_t)$. As discussed in Wouchuk & Cavada (2004), the origin of the shifts $2\chi_r$, $2\chi_t$ is due to the Doppler shift, i.e. to the sonic reverberations. This is why agreement improves when using the iterated function $P_{r1}(q_b)$ as written in (8.11). Having established the way to invert the Laplace transforms we can proceed now to calculate the asymptotic velocity profiles inside each fluid. To this end we need the vorticity generated by each rippled front. To calculate the vorticity, we recall the important fact that tangential momentum across each rippled front is conserved, and this mechanism is responsible of generating a tangential velocity perturbation behind the corrugated shock, see (6.7, 6.8), which in turn is the way vorticity is created; see Wouchuk (2001*a*), Cobos-Campos & Wouchuk (2016) and Wouchuk (2025). The important consequence is that the velocity fields generated by the corrugated fronts are of rotational nature. We recall here the definition of the z- component of vorticity

$$\delta\omega(x,\, y) = \frac{\partial \delta v_y}{\partial x} - \frac{\partial \delta v_x}{\partial y}. \tag{9.10}$$

We must pay attention to the fact that vorticity is only generated at each corrugated shock. Once it is created, in the absence of viscosity, the vorticity attached to the fluid element does not change in time. That is, the time derivative of $\delta\omega$ following the fluid element is zero: $\mathrm{d}\delta\omega/\mathrm{d}\tau = 0$, which, in linear theory, reads $\partial\ \delta\omega/\partial\tau = 0$. That is, the vorticity field is steady state and hence only a function of space coordinates $(x,\, y)$. Let us start with the reflected shock: we define the dimensionless characteristic time $\tau_0(x) = kx/\beta_r$ as the time needed by the reflected shock to arrive at position x. Associated with τ_0, the value of the corresponding variable r is

$$r_0(x) = \frac{kx}{\sinh\chi_r} = \frac{kx}{\beta_r}\sqrt{1-\beta_r^2}. \tag{9.11}$$

Therefore, in order to compute the vorticity at position $(x,\, y)$ we must get the values of the partial derivatives $\partial\delta v_y/\partial x$ and $\partial\delta v_x/\partial y$ at the time τ_0 behind the reflected shock. To this end we use the conservation of tangential momentum across the front, and differentiate with respect to time, following the reflected shock, that is, applying the differential operator $\mathrm{d}/\mathrm{d}\tau = \partial/\partial\tau + \beta_r\partial/\partial x$ at both sides of the equation that defines v_r

$$v_r(\tau) = \frac{U_1 - U}{D_i}\psi_r(\tau). \tag{9.12}$$

After some algebra, the value of $(\partial v/\partial x)_{x_r}$ is readily obtained. The value of $\partial v_x/\partial y$ is easily computed from (6.5). Collecting both results, we get

$$\omega_b(x,\, y) = g_b(x)\sin ky. \tag{9.13}$$

The function $g_b(x)$ is

$$g_b(x) = \Omega_b\hat{p}_r\left(r_b = \frac{kx}{\sinh\chi_r}\right), \tag{9.14}$$

in which the constant Ω_b is given by

$$\Omega_b = \frac{(M_r^2-1)^2}{M_r^2}\frac{\sqrt{\gamma_b M_r^2 - \gamma_b + 1}}{\left[(\gamma_b-1)M_r^2+2\right]^{3/2}}. \tag{9.15}$$

https://doi.org/10.1017/jfm.2025.10740 Published online by Cambridge University Press

It is easy to see that, for a weak incident shock, the vorticity quantity Ω scales like: $\Omega_b \sim z_t^2$. Proceeding similarly with the transmitted shock, we write the vorticity stored inside fluid a

$$\omega_a(x, y) = g_a(x) \sin ky. \tag{9.16}$$

The function $g_a(x)$ is

$$g_a(x) = \Omega_a \hat{p}_t \left(r_a = \frac{kx}{\sinh \chi_t} \right), \tag{9.17}$$

in which the constant Ω_a is given by

$$\Omega_a = \frac{(M_t^2 - 1)^2}{M_t^2} \frac{\sqrt{\gamma_a M_t^2 - \gamma_a + 1}}{\left[(\gamma_a - 1)M_t^2 + 2\right]^{3/2}}. \tag{9.18}$$

Please note that, inside fluid a, the longitudinal cordinate x is negative, i.e.: $x < 0$, and therefore $\chi_t < 0$. Hence, the argument r_a inside $\hat{p}_t$ of (9.17) is positive. There is an important physical meaning of (9.14–9.17) above: the value of the vorticity generated at position x is proportional to the shock pressure perturbations at the time $\tau_0(x)$. In this sense, the vorticity stored in each compressed fluid is a memory of the compressible evolution of the corresponding shock front perturbations since $t = 0+$. What is even more important is that the velocity field in the limit $t \to \infty$ must be consistent with this vorticity field, and hence, it will never be an irrotational field. The irrotationality assumption of the velocity fields will be approximate for an incident shock of negligible intensity.

As each of the shocks separate from the contact surface, their ripples oscillate in time with decaying amplitude. Meanwhile, the shocks fill the space between them with an acoustic field of pressure perturbations in both fluids, $\hat{p}_b(r_b, \chi_b)$, $\hat{p}_a(r_a, \chi_a)$, which also decrease to zero in the asymptotic limit $t \to \infty$. Therefore, when the shocks are very far away, the fluid particles do not experience acceleration any more and the velocity field becomes steady state (Wouchuk & Nishihara 1996, 1997; Wouchuk 2001*a*). Our immediate purpose now is to derive the differential equations that describe the asymptotic velocity fields in both fluids as functions of the spatial coordinates x and y: as has been shown for the first time in Wouchuk (2001*a*), the longitudinal velocity perturbations inside fluid b satisfy the differential equation written immediately below (this equation is obtained by combining the linearised Euler equations) (Wouchuk 2001*a*, 2025)

$$u_b''(x) - u_b(x) = -g_b(x). \tag{9.19}$$

While the tangential velocity perturbations obey the equation

$$v_b''(x) - v_b(x) = g_b'(x). \tag{9.20}$$

Inside fluid a, we have identical equations for $u_a(x)$, and $v_a(x)$

$$u_a''(x) - u_a(x) = -g_a(x), \tag{9.21}$$

$$v_a''(x) - v_b(x) = g_a'(x). \tag{9.22}$$

It is convenient to solve (9.19, 9.21) here to get the spatial profile of the velocity field.

As for the longitudinal velocity $u_b(x)$ inside the light fluid, the solution of (9.19) can be written as the solution of the homogeneous equation plus a particular solution. We propose then

$$u_b(x) = Ae^{-x} + u_{bpart}(x). \tag{9.23}$$

https://doi.org/10.1017/jfm.2025.10740 Published online by Cambridge University Press

As for the particular solution we propose

$$u_{bpart}(x) = \int_{-1}^{+1} h_{bs}(z) \sin \frac{zx}{\sinh \chi_r} \mathrm{d}z. \tag{9.24}$$

Constant A in (9.23) will be determined soon. As for the function $h_{bs}(z)$ entering in u_{bpart}, it can be calculated by plugging (9.24) into the left-hand side of (9.19). We also use (9.14). After simple inspection, we get

$$h_{bs}(z) = \frac{\Omega_b \sinh^2 \chi_r}{z^2 + \sinh^2 \chi_r} f_{rs}(z). \tag{9.25}$$

Thanks to the fact that $\hat{p}_r(r = 0+) = 0$, there is only a sine contribution in the integral decomposition for $\hat{p}_r$, (9.3), which in turn gives only a sine contribution for the integral that defines $u_{bpart}(x)$ in (9.24). Hence, the vanishing of the pressure perturbations behind the reflected shock at $t = 0+$ implies $u_{bpart}(x = 0) = 0$. Therefore, the constant A in (9.23) is $A = u_c^\infty$.

The tangential velocity perturbations are obtained by differentiating (9.23): $v_b(x) = -u_b'(x)$.

The fact that the pressure perturbations vanish asymptotically in time has a profound consequence: given that $\partial \delta\rho/\partial\tau = \partial \delta p/\partial\tau$, because of entropy conservation (Landau & Lifshitz 1986), we deduce that, when the shocks are infinitely apart from the contact surface, the velocity fields of both fluids become incompressible, independently of the values of γ_a, γ_b and M_i. This means that $v(x) = -u'(x)$ in both fluids. The differential equations above can then be integrated inside the interval $0 < x < \infty$ using the Laplace transforms of the functions P_r and P_t, as will be shown soon. Let us multiply both members of (9.21) by $e^{-\sigma x}$, with σ a positive real number yet to be determined . After integration by parts and using the asymptotic incompressibility commented on above, we define, for fluid b, the function $U_b(\sigma)$: (Wouchuk 2001*a*, 2025)

$$U_b(\sigma) = \int_0^\infty u(x) e^{-\sigma x} \mathrm{d}x = \frac{\sigma u_c^\infty - v_{bc}^\infty - \Omega_b \ \sinh \chi_r \ P_r(s_b = \sigma \sinh \chi_r)}{\sigma^2 - 1}, \tag{9.26}$$

where u_c^∞ is the asymptotic dimensionless longitudinal velocity at the contact surface ripple, and v_{bc}^∞ is the dimensionless tangential velocity, also at the position of the unperturbed contact surface ($x = 0$) inside fluid b.

For ideal gases we do not have poles for P_r and thus we do not expect poles for U_b either. This is only possible if the numerator of (9.26) vanishes for $\sigma = 1$. After rearranging terms, this condition leads us to the relationship

$$u_c^\infty - v_{bc}^\infty = \Omega_b \ \sinh \chi_r \ P_r \ (q_b = \chi_r) \equiv F_b, \tag{9.27}$$

where v_{bc}^∞ is the asymptotic tangential velocity at the contact surface inside fluid b. It is only approximately equal to u_c^∞ for a very weak shock, because $F_b \sim 0$ in that limit. The above condition relates the values of u_c^∞ and v_{bc}^∞ to a particular integral of the shock pressure perturbations since $t = 0+$ up to $t = \infty$. An important conclusion is that u_c^∞, v_{bc}^∞ are never exactly equal.

Inside fluid a, we multiply both members of (9.21) by $e^{\sigma} x$ and integrate inside the interval $-\infty < x < 0$. Integrating by parts and proceeding as we did with $U_b(\sigma)$, we arrive at an equation that relates the longitudinal and tangential velocities at the contact surface, but on side a

$$F_a = v_{ac}^\infty + u_c^\infty = \Omega_a \sinh \chi_t P_t(q_a = \chi_t) \equiv F_a, \tag{9.28}$$

https://doi.org/10.1017/jfm.2025.10740 Published online by Cambridge University Press

where v_{ac}^{∞} is the asymptotic tangential velocity at the contact surface, inside fluid a. Once we compute the values of F_a, F_b, we get the value of u_c^{∞}, the purpose of this work.

The procedure to obtain u_c^{∞} from the values of F_a, F_b has been already explained in Wouchuk & Nishihara (1997) but it is briefly recalled here. Thanks to the continuity of pressure at the contact surface, we equate the y components of the Euler equations, on both sides of the contact surface, and write

$$\rho_{af}\frac{\partial v_a(\tau)}{\partial \tau} = \rho_{bf}\frac{\partial v_b(\tau)}{\partial \tau}. \tag{9.29}$$

If we integrate from $\tau = 0$, up to $\tau = \infty$, we get

$$R(v_{ac}^{\infty} - v_{a0}) = v_{bc}^{\infty} - v_{b0}, \tag{9.30}$$

where v_{b0}, v_{a0} are the initial tangential velocities behind the reflected and transmitted shocks, respectively. Combining (9.27–9.30), we solve for the normal velocity

$$u_c^{\infty} = \frac{v_{b0} - Rv_{a0}}{R+1} + \frac{RF_a - F_b}{R+1}. \tag{9.31}$$

We see that that the asymptotic normal velocity is composed of the two terms indicated above. If there were no vorticity stored inside each fluid, the quantities F_a, F_b would vanish, and hence only the term containing v_{a0}, v_{b0} would be enough to compute u_c^{∞}. This is why we like to call it u_{irrot}, as it would be the only contribution for a perfectly irrotational velocity field

$$u_{irrot} = \frac{v_{b0} - Rv_{a0}}{R+1}. \tag{9.32}$$

Of course, this will never happen, because the term containing F_a, F_b is important in the general case, especially at high compressions. Here, we see the need to calculate the Laplace transforms P_r, P_t.

By the same token, we define

$$u_{rot} = \frac{RF_a - F_b}{R+1}, \tag{9.33}$$

and we formally write

$$u_c^{\infty} = u_{irrot} + u_{rot}. \tag{9.34}$$

To compute u_{rot}, we need F_a, F_b. Here, F_a is calculated using the iterated function P_{t1}, given in (8.6), and F_b is evaluated using P_{r1} as written in (8.11). In Wouchuk (2001*a*) a highly accurate iterative procedure to compute F_a, F_b was developed, by solving exactly the boundary conditions at both shocks and at the contact surface. However, that iteration scheme is of a rather complicated algebraic structure. It is complicated system of coupled functional equations for $F_{a1}(q_a)$, $F_{a2}(q_a)$, and $F_{b1}(q_b)$, $F_{b2}(q_b)$, but the procedure to solve those equations in Wouchuk (2001*a*) did not involve any approximation like the RPA used here. Take a look, for instance, at equations (65) and (66) of Wouchuk (2001*a*).

The physical meaning of the quantities F_a, F_b is simple: they represent the fluxes of the vorticity fields stored inside each fluid.

10. Comparison with the numerical work of Yang *et al.* (1994)

It is customary to compare, as we did in the past, with Yang *et al.* (1994). In this section we start comparing with the linear simulations of Yang *et al.* (1994). Before comparing we set some notation.

https://doi.org/10.1017/jfm.2025.10740 Published online by Cambridge University Press

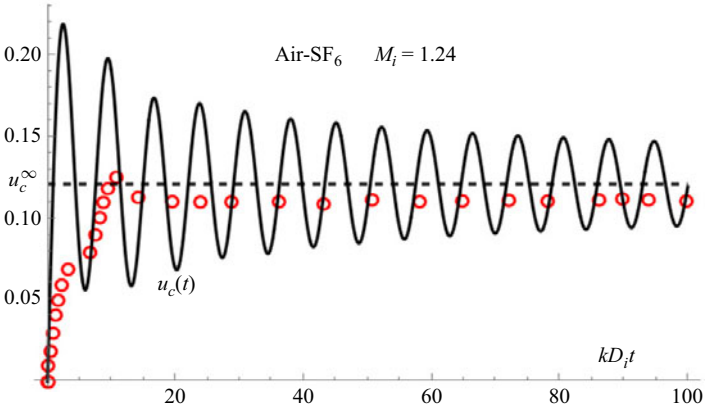


Figure 8. The black continuous curve is calculated with (10.1). Red circles are from figure 7 of Yang *et al.* (1994), for the gases and shock Mach number indicated. The horizontal dashed black line is the terminal velocity u_c^∞ calculated with (9.34).

As shown in previous work (Wouchuk & Nishihara 1996), the normal velocity at the contact surface can be written, as a function of time, as

$$u_c(\tau_b) = u_c^\infty \int_0^{\tau_b} J_0(t)\mathrm{d}t + \sum_{n\geqslant 0} \omega_{b2n+1} \left(J_{2n+1}(\tau_b) + 2 \sum_{k\geqslant 0}^{n-1} J_{2k+1}(\tau_b) \right), \qquad (10.1)$$

where the coefficients $\omega_{b\nu}$ have been defined before; take a look, for instance, immediately after (4.13). The function $J_\nu(t)$ is the ordinary Bessel function of order ν. In figure 8 we compare our calculation of the ripple's normal velocity as a function of time, (10.1) with the linear simulations of Yang *et al.* (1994).

In figure 8 we compare (10.1) with figure 7 of Yang *et al.* (1994). Our solution has been constructed including up to ω_{51}^b inside the corresponding sums of (10.1). Besides this, we also compare below with table I of Yang *et al.* (1994). Table 1 is constructed in this way: for each pair of values (R_0, s), the upper number in a row corresponds to the result of (9.31), while the lower one is the value shown in table I of Yang *et al.* (1994).

From table 1 we see that our predictions are consistent with those of Yang *et al.* (1994), except for a few cases when the shock is very strong and/or γ values are very different. The worst case scenario seems to be when $\gamma_a = 3.0$, $\gamma_b = 1.5$, for a very strong shock ($s \sim 1.0$), with $R_0 = 1.1$ for which the result of Yang *et al.* (1994) seems to indicate the proximity of freeze-out (Mikaelian 1991). We recall here again that the functionals (7.2, 7.5) are actually approximate equations, obtained with the RPA supported by figure 3, which motivated us to make $F_{b1}(q_b) \sim F_{b2}(q_b)$, and hence to approximate $J_{cb}(q_b) \sim 0$. Hence, even though we have obtained the exact solution of (7.2, 7.5), the equations themselves are only an approximation to the true equations satisfied by P_r and P_t. The RPA might break down when the Mach number increases without bound, or when the γ values are very different on each side of the contact surface. We will later estimate the relative error (which will be called η_c) incurred in the calculation of u_c^∞, because of the assumption $J_c(q_b) \sim 0$. We will study the dependence of η_c as a function of s and as a function of the γ values. So far, the iteration procedure used in Wouchuk (2001*a*) gives more accurate estimates of u_c^∞ than our estimate here. The reason seems to be clear: in Wouchuk (2001*a*), the system of functional equations embodied in (6.5 and 6.6) of that work are exact, as they involve the complete/exact boundary conditions at the shocks and the contact surface. This fact

https://doi.org/10.1017/jfm.2025.10740 Published online by Cambridge University Press

s	$R_0 = \rho_{a0}/\rho_{b0}$				
	1.1	2.0	4.0	8.0	16.0
			(*a*)		
1.0	0.005375	0.03563	0.0654	0.0852	0.088
	0.0040	0.0310	0.064	0.094	0.11
0.5	0.0175	0.1042	0.1507	0.1520	0.1304
	0.015	0.093	0.1400	0.15	0.13
0.05	0.002093	0.01246	0.01808	0.01839	0.01599
	0.0021	0.0120	0.0180	0.0180	0.016
			(*b*)		
1.0	0.016	0.09635	0.1435	0.1494	0.1316
	0.014	0.089	0.14	0.1600	0.1400
0.5	0.00078	0.0515	0.0748	0.0761	0.066
	0.0078	0.0046	0.0720	0.0750	0.0650
0.05	0.0081	0.00466	0.00676	0.00687	0.00597
	0.0078	0.0046	0.0067	0.0068	0.0060
			(*c*)		
1.0	0.0029	0.0427	0.0607	0.0603	0.478
	−0.0038	0.0710	0.1400	0.1900	0.0514
0.5	0.0159	0.081	0.089	0.088	0.10357
	0.0040	0.0064	0.1000	0.1100	0.0950
0.05	0.0013	0.0057	0.01058	0.010527	0.008982
	0.0012	0.0073	0.0100	0.0100	0.0089

Table 1. Ripple terminal velocities as given by (9.31) and the numerical simulations by Yang *et al.* (1994). The upper number in each entry is the result of this work and the lower one is the result shown in Table 1 of Yang *et al.* (1994). The adiabatic exponents are: (*a*) $\gamma_a = \gamma_b = 1.1$, (*b*) $\gamma_a = \gamma_b = 3.0$, (*c*) $\gamma_a = 3.0$, $\gamma_b = 1.5$.

explains the good agreement observed between Wouchuk (2001*a*) and Yang *et al.* (1994). The solution presented here for P_r and P_t is appealing because of its simplicity, but is unfortunately tainted with an approximation that might break down for very strong shocks and/or very different gamma values.

To be clearer, our solution for $P_t(q_a) = \lambda_{a1}(q_a)$, even though it is the exact solution of (7.5), predicts $P_t(\chi_t) = 0$ and hence, $F_a = 0$, which is unphysical. This result is incorrect taking into account that F_a becomes important for strong shocks and very different γ values. In fact, following the iteration procedure explained in Wouchuk (2001*a*), for $\gamma_a = 3.0$, $\gamma_b = 1.5$, $s \sim 1.0$, we get, after some iterations: $F_a \sim 0.072 \neq 0$, $u_c^\infty \sim -0.0383$ in better agreement with Yang *et al.* (1994). The problem is actually with the approximation that supports (7.5) itself. Nevertheless, as will be seen later, reasonable agreement with experiments is obtained when analysing the ripple's growth, within the time domain of validity for a linear theory, for relatively weak shocks.

It is important that we also compare with figure 11 of Yang *et al.* (1994).

In order not to overcrowd the figure, each case is shown as a separate plot in both figure 9 and figure 10. The values of γ and R_0 are taken from Yang *et al.* (1994). The blue line is the prediction of u_c^∞ here. Red circles are the simulation results of Yang *et al.* (1994). The black, dashed line is Fraley's prediction given by (13.2), presented in Fraley (1986); see the explanation near (13.2) for details. The blue line is always given by (9.31)

In all the cases shown in figure 9, and figure 10 the terminal velocity has been calculated with the RPA, and shown as the continuous blue line, as given by (9.31). The broken, black line is given by the formula presented by Fraley (1986), according to the expressions derived by K. Mikaelian in Mikaelian (1991), which is shown in this work as (13.2). Red empty circles are from Yang *et al.* (1994).

https://doi.org/10.1017/jfm.2025.10740 Published online by Cambridge University Press

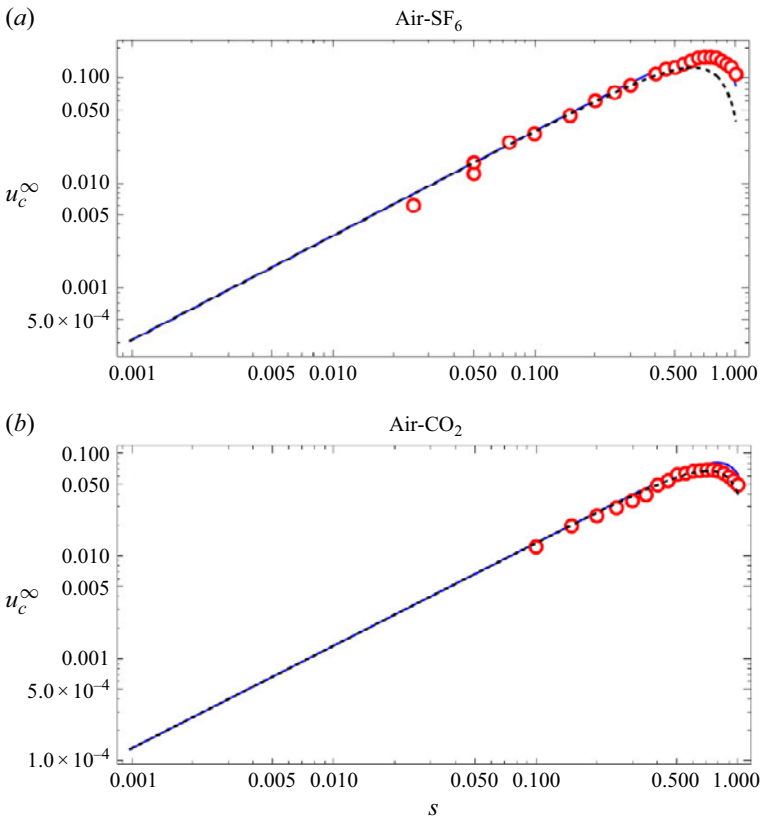


Figure 9. Terminal velocity as a function of shock strength s for the gases indicated. Blue line is given by (9.31). Black dashed line is Fraley's formula, (13.2), and red, empty circles are from figure 11 of Yang *et al.* (1994).

Red circles in figures 9–10 have been measured from figure 11 of Yang *et al.* (1994). In general, we see a reasonable agreement between our prediction and the numerical results of Yang *et al.* (1994), despite the unphysical prediction $F_a = 0$. It is also important to note is that our prediction sensibly agrees with Fraley's formula, as will be shown later on.

11. Weak shock limit

It is important to discuss the behaviour of the asymptotic velocity for very weak incident shocks.

To understand the behaviour of the terminal velocity in the limit $z_i \to 0$, it is convenient to analyse the behaviour of the bulk vorticity quantities F_a, F_b. To this end, it is very convenient to recall the representations as infinite series of decaying exponentials for P_r, P_t, with the aid of (5.11)

$$P_r(q_b) := \sum_{n=0}^{\infty} D_{b2n+1} \frac{e^{-(2n+1)q_b}}{\cosh q_b}, \tag{11.1}$$

$$P_t(q_a) := \sum_{n=0}^{\infty} D_{a2n+1} \frac{e^{-(2n+1)q_a}}{\cosh q_a}. \tag{11.2}$$

https://doi.org/10.1017/jfm.2025.10740 Published online by Cambridge University Press

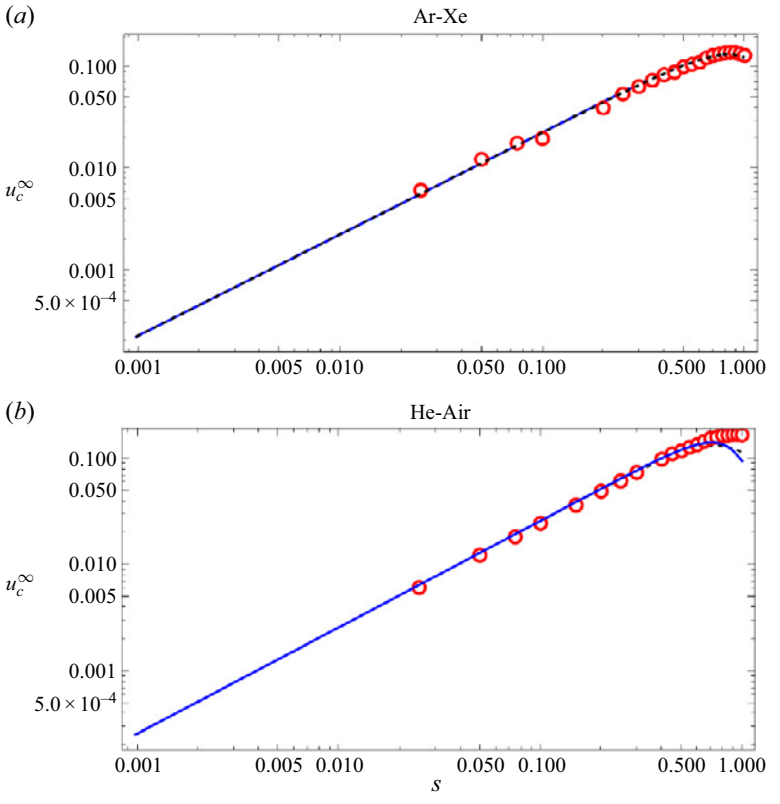


Figure 10. Terminal velocity as a function of shock strength s for the gases indicated. Blue line is given by (9.31). Black dashed line is Fraley's formula, (13.2), and red, empty circles are from figure 11 of Yang *et al.* (1994).

We recall the formulas for F_a, F_b, given in (9.28, 9.27)

$$\begin{aligned} F_a &= -\Omega_a \sinh\chi_t \;\; P_t(\chi_t), \\ F_b &= \Omega_b \sinh\chi_r \;\; P_r(\chi_r). \end{aligned} \tag{11.3}$$

With the aid of Supplementary materials, it can be seen that $|D_{bv}| < |D_{b1}|$. Hence, we can write

$$|F_b| < \Omega_b \sinh\chi_r |D_{b1}| S_g(\chi_r)/\cosh\chi_r, \tag{11.4}$$

where the function $S_g(q_b)$ is the sum of a geometric series

$$S_g(q_b) = \sum_{n=0}^{\infty} e^{-(2n+1)q_b} = \frac{e^{+q}}{e^{2q}-1}. \tag{11.5}$$

Plugging in the above results into (11.3), we get, for the reflected shock

$$|F_b| < \Omega_b \sinh\chi_r |D_{b1}| S_g(\chi_r)/\cosh\chi_r. \tag{11.6}$$

In order to take the weak shock limit of the right-hand side of the above inequality, we recall the scaling of (2.30): $e^{-\chi_r} \sim \sqrt{z_i}$, if $z_i \ll 1$. Besides, coefficient D_{b1} is linear in z_i: $D_{b1} \sim z_i$. From (9.15), we see that Ω_a, $\Omega_b \sim z_i^2$ for very weak shocks. Plugging in all these scalings into the right-hand side of (11.6), we deduce: $F_b \sim z_i^{7/2}$. And analogously for F_a. On the other hand, it is not difficult to see that $u_{irrot} \sim z_i$. Therefore, for very weak

https://doi.org/10.1017/jfm.2025.10740 Published online by Cambridge University Press

shocks, the contribution of the bulk vorticity quantities F_a, F_b can be safely neglected in comparison with u_{irrot}. Therefore, when considering the weak shock limit of u_c^{∞}, it is enough to expand u_{irrot} up to third order and neglect the vorticity contribution. The expansion coefficients of u_{irrot} are also too lengthy to be written here and the interested reader will find them inside Supplementary materials. It is convenient that the interested reader takes a look inside Supplementary materials, before delving into the corresponding Mathematica file.

12. Comparison with Richtmyer's impulsive formula. Weak shock limit of (9.31)

In his pioneering work, Richtmyer (1960) showed for the first time an analytical/simple formula with which to reproduce the value of the asymptotic velocity as given by his numerical simulations. The formula is based on the assumption that the incident shock induces an infinite acceleration to the contact surface during a vanishingly small amount of time, thus imparting to it a finite velocity jump. This approximation is called an impulsive formula. In our notation, the impulsive formula reads

$$u_{impulsive} = \frac{R-1}{R+1}\frac{U}{D_i}\,\psi_0^*, \tag{12.1}$$

where ψ_0^* is the contact surface ripple amplitude after the incident shock refracts

$$\psi_0^* = \left(1 - \frac{U}{D_i}\right)\psi_0. \tag{12.2}$$

It is well known that the impulsive formula almost agrees with the observed/calculated asymptotic velocity for very weak shocks, but large discrepancies might be expected for shocks of finite/large Mach and/or highly compressible fluids.

13. Comparison with G. Fraley's formula (Fraley 1986)

13.1. *Shock perturbation dynamics*

In Wouchuk & Cavada (2004), we have made a detailed analysis of Fraley's original work on the RMI, and showed the equivalence between his approach and ours. Even though he obtained a system of functional equations of a different nature, his equations are totally equivalent to our functional (7.2, 7.5). Whether his equations can be easily solved with a similar procedure as presented here is yet to be seen.

Besides, when delving into Fraley's algebra we will soon realise that the Doppler effect at each shock is the physical mechanism responsible for the appearance of his functional equations. Given that our model is physically and mathematically equivalent to Fraley's, we conclude that the shift inside the arguments of our functions P_r, P_t are also a consequence of the Doppler shift experienced at each shock front respectively.

13.2. *Terminal velocity of the contact surface ripple*

Having established that our model equations describing the shock pressure perturbation evolution and Fraley's are equivalent, it remains to compare Fraley's prediction for u_c^{∞}, written as (46) in Fraley (1986), with our result here written in (9.31). Unfortunately, Fraley has not given an explicit, easy to use formula. But Mikaelian in Mikaelian (1991) did. In fact, K. Mikaelian took considerable effort in developing Fraley's difficult (46) and presented it as (16) in Mikaelian (1991). Details can be found in Mikaelian (1991). Fraley normalised the ripple velocity with the post-shock speed of the contact surface (Δv in Fraley and Mikaelian's notation, but U in our notation.) For ease when discussing the

https://doi.org/10.1017/jfm.2025.10740 Published online by Cambridge University Press

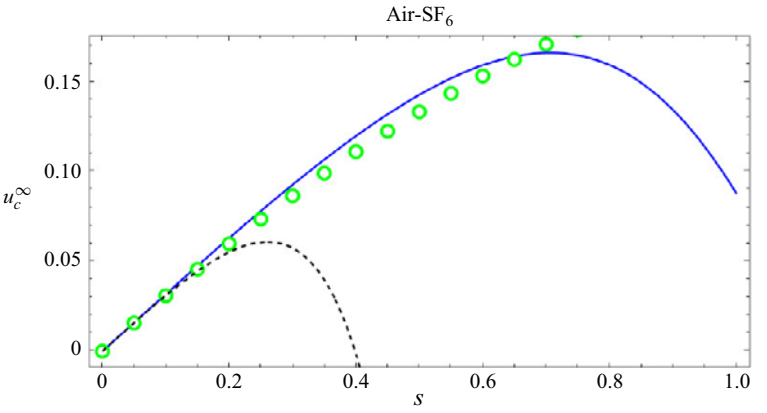


Figure 11. Blue line is u_c^∞ given by (9.31). Green, empty circles are given by the impulsive formula, and the black, dashed line is the third order expansion of u_{irrot} which can be found inside Supplementary materials.

results, we write below Mikaelian's explicit formula, with the notation used in this work. Let u_F be the dimensionless value of the ripple's asymptotic velocity, as calculated by Fraley and Mikaelian. We have, according to (16) of Mikaelian (1991) and recalling that we defined $R = \rho_{af}/\rho_{bf}$

$$u_F = \frac{\delta v_{xi}}{k\psi_0 U} = \frac{Ra_1 - a_2}{R+1}. \tag{13.1}$$

But in order to compare with Yang *et al.* (1994), we must renormalise Fraley's result with the incident shock speed D_i. To this end, we define

$$u_{FC} = \frac{U}{D_i} u_F, \tag{13.2}$$

where subscript FC stands for Fraley corrected. This is the quantity that is shown in figure 10, together with u_c^∞ calculated in (9.31). The quantities a_1, a_2 are given explicitly in the Appendix of Mikaelian (1991). We see a close analogy between the expression for u_F above and our u_c^∞. It seems as if a_1 were related to $F_a - v_{a0}$, while a_2 seems to be related to our $F_b - v_{b0}$. They are not exactly equal, however. In figure 10(a), we show the prediction of u_{FC} as a function of the shock intensity parameter s, shown as the black-dashed curve, while the blue solid line is our result here. Red dots are from Yang *et al.* (1994), for the air–F_6 case. Figure 10(b) is the same, but for air–CO_2. Figure 11(a) is the same as figure 10(a), but for Ar–Xe. Finally, figure 11(b) is for He–Air.

We see that u_c^∞ and u_{FC} predict almost identical results, for shocks of moderate to large Mach numbers. In the very weak shock limit both formulas agree, as expected. Our results here need the definitions of four auxiliary functions: $\lambda_{a1}(q_a)$, $\lambda_{a2}(qa)$, $\lambda_{b1}(q_b)$, $\lambda_{b2}(q_b)$, plus quantities Ω_a, Ω_b. Mikaelian's expressions for u_F seem to be shorter to write than ours. Nevertheless, Mikaelian had also the need to define several auxiliary quantities: his quantity x, which is actually equal to our $1 + z_r$, plus his other quantities: α_A, α_B, ϵ_B. Which one to use is more a matter of taste/convenience, given that for shocks of weak/moderate strength, both formulas predict almost identical results. From figure 10 it is clear that u_c^∞ and u_{Fc} give almost the same values, and the difference is not discernible with a double logarithmic scale. To see how much they agree/differ with/from each other, we show both quantities as a function of s for the gases indicated in tables 2, 3, 4 and 5. We see that $u_c^\infty \neq u_{Fc}$ in general, but they predict values quite close to each other.

https://doi.org/10.1017/jfm.2025.10740 Published online by Cambridge University Press

s	u_c^∞	u_{FC}
0.005	0.016	0.01599
0.5	0.0155	0.1275
0.75	0.2196	0.1235
0.80	0.2297	0.1129
0.85	0.2382	0.099
1.0	0.2468	0.041

Table 2. Comparison between u_c^∞ and u_{FC} for the air–SF_6 configuration.

s	u_c^∞	u_{FC}
0.005	0.006917	0.006910
0.5	0.06613	0.05957
0.75	0.0919	0.0683
0.80	0.09035	0.06660
0.85	0.09537	0.06641
1.0	0.09551	0.04046

Table 3. Comparison between u_c^∞ and u_{FC} for the air–CO_2 configuration.

s	u_c^∞	u_{FC}
0.005	0.0114	0.0114
0.5	0.1166	0.1051
0.75	0.171	0.132
0.80	0.1806	0.134
0.85	0.1895	0.134
1.0	0.21008	0.1263

Table 4. Comparison between u_c^∞ and u_{FC} for the Ar–Xe configuration.

In Supplementary materials we explicitly show the Mathematica routine that has been used to calculate figure 10, in which the formula for u_{FC} is also included. It is convenient to take a look at the Readmefirst files before delving into the Mathematica files. Inside Supplementary materials, the interested reader will also find the explicit calculation of the third-order weak shock expansion for u_{irrot}, (9.32). It is clear from the results presented here that a simple formula like the impulsive prescription (12.1) is not possible to obtain at the moment. If we want to describe regimes of high compression, it might be necessary to deal either with u_F or with u_c^∞.

From tables 2–5 we see that Fraley's formula and our expression u_c^∞ coincide in the very weak shock limit, as expected, and stay near each other for stronger shocks, but they are never exactly equal.

14. Contact surface ripple growth

We discuss now the growth of the contact surface ripple in time. It is necessary that we review here some concepts of the Laplace transform theory. Even though comparison of

https://doi.org/10.1017/jfm.2025.10740 Published online by Cambridge University Press

s	u_c^∞	u_{FC}
0.005	0.01316	0.01314
0.5	0.1342	0.11146
0.75	0.19947	0.13409
0.80	0.2118	0.1330
0.85	0.2238	0.1304
1.0	0.2577	0.11160

Table 5. Comparison between u_c^∞ and u_{FC} for the He– air configuration.

the terminal velocity with simulations is straightforward, experiments only measure the ripple's amplitude at the contact surface as a function of time. In order to compare with the published experiments we need to integrate in time the normal velocity given by (10.1). We do this integration carefully below. Before delving into the full calculation, we review here some useful results of the theory of the Laplace transform.

Let $f(t)$ a function of time, whose Laplace transform is $F(s)$. According to the so called Tauberian theorem (see for instance, page 134 of Sneddon 1972), the following result is valid.

If $\lim_{t\to\infty} f(t) = L$ exists, then

$$L = \lim_{s\to 0} s\ F(s). \tag{14.1}$$

We will also need the Laplace transform of a time integral: let $g(T) = \int_0^T f(t)\mathrm{d}t$. The Laplace transform of g is given by (Sneddon 1972)

$$G(s) = \frac{F(s)}{s}, \tag{14.2}$$

where $F(s)$ is the Laplace transform of $f(t)$. The above results will be necessary to determine the asymptotic ripple's amplitude growth in linear theory. Let us recall that the dimensional velocity at the contact surface ripple is given by

$$\delta v_{xc}(t) = k\psi_0 D_i\ u_c(t). \tag{14.3}$$

Hence, we must integrate in time the equation

$$\frac{\mathrm{d}}{\mathrm{d}t}\psi_c(t) = k\psi_0 D_i\ u_c(t). \tag{14.4}$$

In figure 11 we show the ripple's amplitude as a function of time $u_c(t)$, calculated with 21 terms inside the corresponding Bessel series. We also show the terminal velocity u_c^∞ with a dashed horizontal line and have shaded with light-range colour the area between $u_c(t)$ and u_c^∞. If we multiply and divide (14.4) by c_{bf}, we can formally write

$$k\psi_c(\tau_b) = k\psi_0^* + k\psi_0\ \frac{D_i}{c_{bf}}\int_0^{\tau_b} u_c(t)\ \mathrm{d}t. \tag{14.5}$$

The amplitude ψ_0^* is the post-shock ripple amplitude at $t = 0+$. If we add and subtract u_c^∞ inside the integrand of the above equation, we arrive at

$$k\psi_c(\tau_b) = k\psi_0^* + k\psi_0\frac{D_i}{c_{bf}}\int_0^{\tau_b}\left[u_c(t) - u_c^\infty\right]\ \mathrm{d}t + k\psi_0\frac{D_i}{c_{af}}u_c^\infty\tau_b. \tag{14.6}$$

https://doi.org/10.1017/jfm.2025.10740 Published online by Cambridge University Press

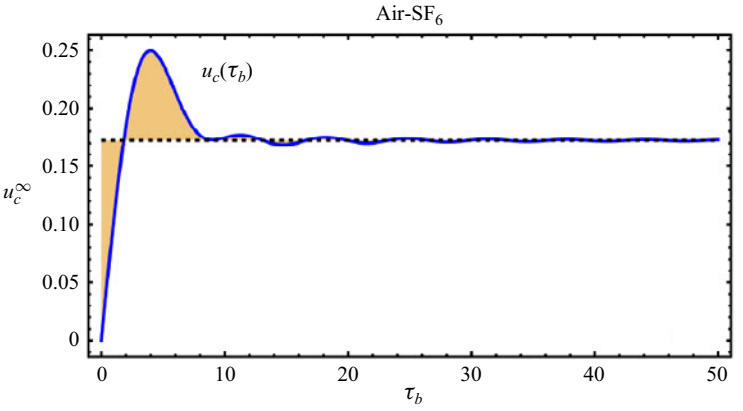


Figure 12. Contact surface ripple velocity as a function of time for the gases indicated with $M_i = 1.45$. The horizontal dashed line is the terminal velocity, u_c^∞. The area between $u_c(\tau_b)$ and u_c^∞ has been shaded to properly follow the discussion in the text.

The Laplace transform of $u_c(\tau_b)$ is given by

$$U_c(q_b) = -\frac{J_c(q_b)}{\sinh q_b}. \tag{14.7}$$

Besides, we recall that $u_c^\infty = -J_c(q_b = 0)$.

Hence, after using (14.1, 14.2), applying L'Hopital's rule and rearranging terms, we get

$$\psi_c(t) = \psi_\infty + \delta v_{xc}^\infty \quad t, \tag{14.8}$$

where we have defined an offset amplitude ψ_∞

$$\psi_\infty = \psi_0^* - \frac{D_i}{c_{bf}} J_c'(0)\,. \tag{14.9}$$

Equation (14.8) above can be rewritten in the alternative form

$$k\psi_c(t) = k\psi_\infty + k\delta v_{xc}^\infty\, t. \tag{14.10}$$

Equivalently, this last equation can be recast in the following form, useful for later discussion:

$$k\psi_c(\tau_b) = k\psi_\infty + k\psi_0 \frac{D_i}{c_{bf}} u_c^\infty \tau_b. \tag{14.11}$$

In figure 13 we show the ripple amplitude $\psi_c(\tau_b)$ for the pre-shock conditions of the experiments of Vandenboomgaerde *et al.* (2014), and for the conditions of the long wavelength experiment of Jacobs & Krivets (2005) for Vandenboomgaerde *et al.* (2014) $M_i = 1.45$, and $M_i = 1.292$, respectively. The red curve is the result of (14.5). The black, dashed line is the asymptotic function given by (14.8). The red curve is calculated with the series of Bessel functions, including up to ω_{b51}. We see some gentle oscillations for small times, which is the effect of the sound waves radiated by the shocks when the shocks are still very near the contact surface. After this transient finished, the red line approaches the asymptote given by the black, dashed line, as predicted by (14.8). This asymptotic behaviour is only valid well before nonlinearity becomes important because, for very large times, growth is known to be reduced due to nonlinear effects.

https://doi.org/10.1017/jfm.2025.10740 Published online by Cambridge University Press

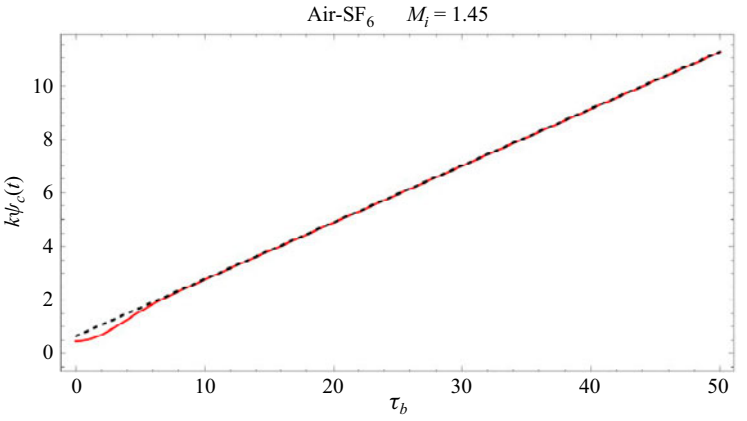


Figure 13. Contact surface ripple amplitude as a function of time for the experiments of Vandenboomgaerde *et al.* (2014). Red continuous line is the solution given by the Bessel series, while the black dashed line is the asymptotic scaling (14.11).

15. Comparison with experiments

15.1. *Experiments of Vandenboomgaerde et al.* (2014)

In this subsection we analyse in detail the experiments presented in Vandenboomgaerde *et al.* (2014). The incident shock comes from air and hits the contact surface separating air from SF_6. The authors studied two cases with equal Mach number and corrugation wavelength but differing only in the initial amplitudes. (Hence, these experiments qualify for the discussion supporting figure 13 above.)

It is convenient to succinctly describe the experiments case by case. The incident shock Mach number is $M_i = 1.45$, which gives us: $s = 0.5626$. Two initial amplitudes were studied: $\psi_{01} = 0.306$cm, and $\psi_{02} = 0.918$cm and the wavelength is $\lambda = 8$cm. For these pre-shock conditions, our calculations predict: $u_c^\infty = 0.173042$. We can thus calculate, for the terminal velocities for both initial conditions, in dimensional units.

(i) Case 1. The initial amplitude of this case is $\psi_{01} \sim 0.306$mm, which gives us: $k\psi_{01} = 0.24 < 1$. The experimentally measured velocity of the incident shock is $D_i = 497.6\ \mathrm{m\ s^{-1}}$ (M. Vandenboomgaerde, personal communication). The dimensionless terminal velocity for this case is: $u_c^\infty = 0.1531$ We thus get for the dimensional terminal velocity

$$\delta v_{xc1}^\infty = 0.24 \times 497.6 \times u_c^\infty \sim 18.312\ \mathrm{m\ ms^{-1}} = 1.8312\ \mathrm{cm\ ms^{-1}}. \tag{15.1}$$

This value is consistent with figure 14(*a*), which is figure 5(*a*) of Vandenboomgaerde *et al.* (2014). The offset amplitude for this case is $\psi_\infty = 0.214242$ cm. The post-shock contact surface velocity is equal to

$$U = D_i \frac{U}{D_i} = D_i \frac{z_t}{\gamma_a M_t M_i} = 36.62\ \mathrm{cm\ ms^{-1}}. \tag{15.2}$$

For this case, the post-shock Atwood number is $A_{Tf} = 0.7337$. Collecting the above results, we get the impulsive prescription for Case 1: $\delta v_{imp1} = 2.5278\ \mathrm{cm\ ms^{-1}}$, which is near to our value, because the shock is quite weak.

https://doi.org/10.1017/jfm.2025.10740 Published online by Cambridge University Press

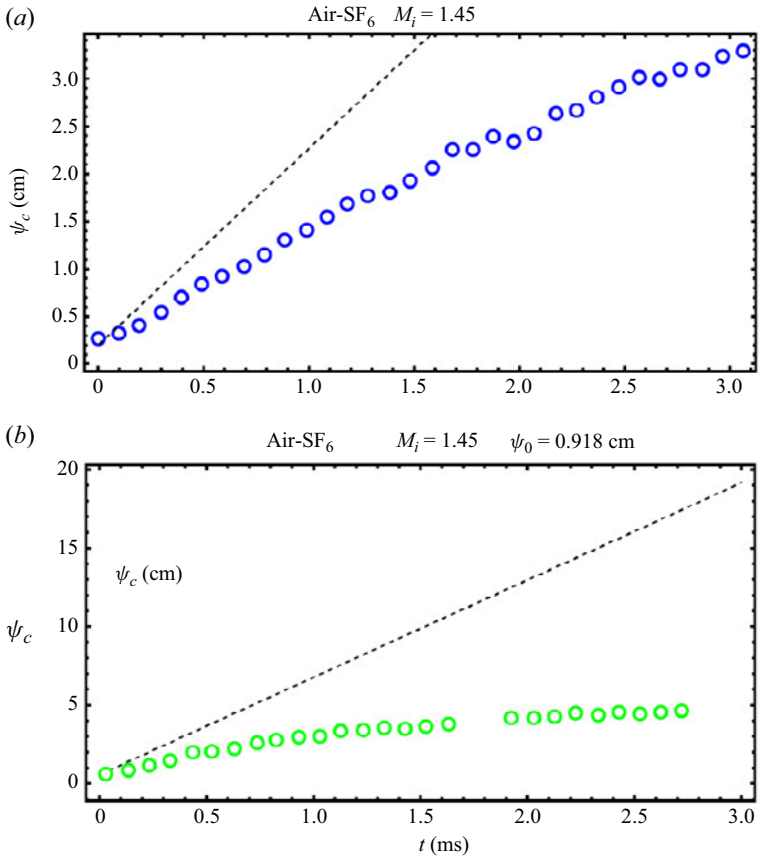


Figure 14. (*a*) Contact surface ripple amplitude as a function of time for case 1 of Vandenboomgaerde *et al.* (2014) which has $\psi_0 = 0.306$ cm. Blue empty circles are the experimental measurements. Black solid line is ψ_c from (14.8). (*b*) Same as (*a*) but for case 2, for which the experimental measurements are shown as green empty circles.

(ii) Case 2. The initial amplitude of this case is $\psi_{02} = 0.918$ cm, which gives $k\ \psi_{02} = 0.721$, $\delta v^{\infty}_{xc2} = 0.0249.18 \times 54.936 \times u^{\infty}_c \sim 5.4936$ cm ms^{-1}. For this case, we get: $\delta v_{imp2} = 7.58338$ cm ms^{-1}, also near to our $\delta\ v^{\infty}_{xc2}$ for the same reason as with Case 1.

The time evolution of Case 1 is shown in figure 14(*a*), and that of Case 2 in figure 14(*b*). In figure 14(*a*), the dashed black line is ψ_c from (14.8). Blue empty circles are from the experiments of Vandenboomgaerde *et al.* (2014), i.e. their figure 5(*a*). Correspondingly, in figure 14(*b*) we show Case 2 of Vandenboomgaerde *et al.* (2014).

Case 1 has a relatively large value for the nonlinearity parameter $k\ \psi_{01} = 0.24$, meaning that nonlinear effects will show up relatively early. This is clearly seen in figure 14(*a*) with the experimental results growing much slower than linear in time. For this experiment we also have $\psi^*_{01} \sim 0.218984$ cm. Besides, the offset amplitude for this case is $\psi_{\infty 1} \sim 0.22437$ cm.

Vandenboomgaerde *et al.* have carefully discussed the onset of nonlinearity for their experiments and considered the criterion $k\psi_c(t_{NL}) \sim 1$ to mark the onset of nonlinearity at a characteristic 'nonlinearity time' t_{NL}. If we use this criterion inside (14.8), we get, for case 1: $t_{NL1} = 0.5133$ ms, while for case 2: $t_{NL2} = 0.1019$ ms. Both values are consistent

https://doi.org/10.1017/jfm.2025.10740 Published online by Cambridge University Press

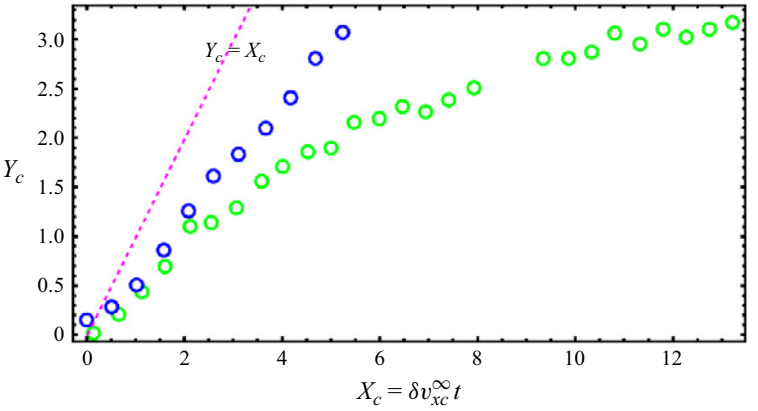


Figure 15. Reduced amplitude Y_c plotted against dimensionless time X_c, according to (14.10) for the experiments of Vandenboomgaerde *et al.* (2014).

with figure 14. For times larger than the t_{NL} characteristic time, the experimental data seem to showa kind of logarithmic growth. Hence linear theory might not be applicable beyond t_{NL}.

There is still an interesting way to show both cases in one single graph, considering the discussion that led us to figure 13, namely, (14.10). The idea is to plot (14.10) for both experiments in a single graph. To this scope, we define the reduced ripple amplitude: $Y_c = k(\psi_c - \psi_\infty)$, plot it against the dimensionless time $X_c = k\delta v_{xc}^{\infty}\, t$ and show Y_c against X_c. This is shown in figure 15. If the growth were only linear, both sets of experimental points would align along the bisectrix $Y_c = X_c$, but once nonlinear effects become important, the experimental points separate from that bisectrix, as is evidenced in figure 15.

We proceed next with the analysis of the experiments of Liu *et al.* (2018).

15.2. *Experiments of Liu et al.* (2018)

We study in detail the case that the authors called 20-1. These experiments have also been done for air–SF_6 and have $\lambda = 20$ mm, $\psi_0 = 1$ mm In what follows, we refer to the experimental points shown in their figure 4, under the heading first harmonic, corresponding to their case 20-1.

The wavenumber is $k = 0.314$, thus giving: $k\psi_0 = 0.314$, which is not much less than 1, implying that a linear theory calculation will run short soon to in order to accurately describe the ripple's growth for large times. The incident shock speed is $D_i = 384.7\ \mathrm{mm\,s^{-1}}$. The velocity of the compressed contact surface is $U = 75\ \mathrm{mm\,s^{-1}}$. Our prediction of the dimensionless terminal velocity is $u_c^{\infty} = 0.1108$. We thus get $\delta v_{xc}^{\infty} \sim 13.396\ \mathrm{mm\,s^{-1}}$, which is consistent with the value the authors report: $v_{Liu} \sim (11 \pm 2.06)\ \mathrm{mm\,s^{-1}}$. We obtain a relative difference of the order of 21 % higher than theirs. For these experiments, we get an offset amplitude $\psi_\infty = 0.823$ mm, and a post-shock ripple amplitude $\psi_0^* = 0.8215$ mm. The impulsive model gives $\delta v_{imp} \sim 12.1433\ \mathrm{mm\,s^{-1}}$, which is quite near our value because the shock is quite weak ($M_i = 1.22$). For the onset of nonlinearity we get $t_{NL} \sim 0.176$ s, which is evidenced in figure 16, where we see that the ripple growth starts to become nonlinear at $t = 0+$, because $k\psi_0 = 0.314 > 1$. The comparison of these experiments with the theoretical predictions of this work is shown below in figure 16.

https://doi.org/10.1017/jfm.2025.10740 Published online by Cambridge University Press

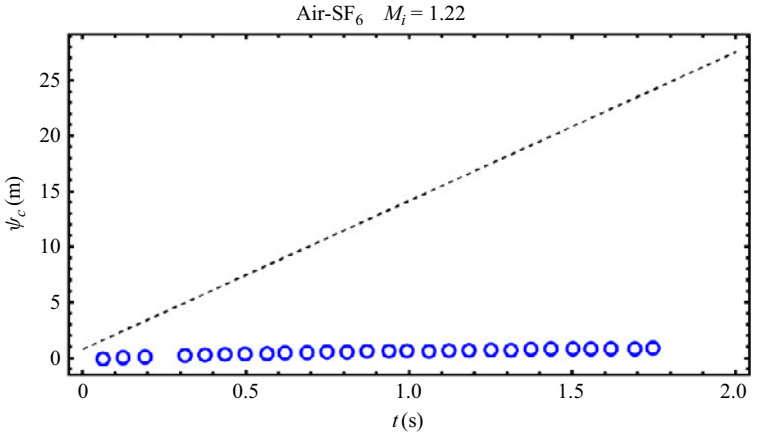


Figure 16. Ripple amplitude growth for the experiments shown in figure 4 of Liu *et al.* (2018). Black line is our prediction (14.8).

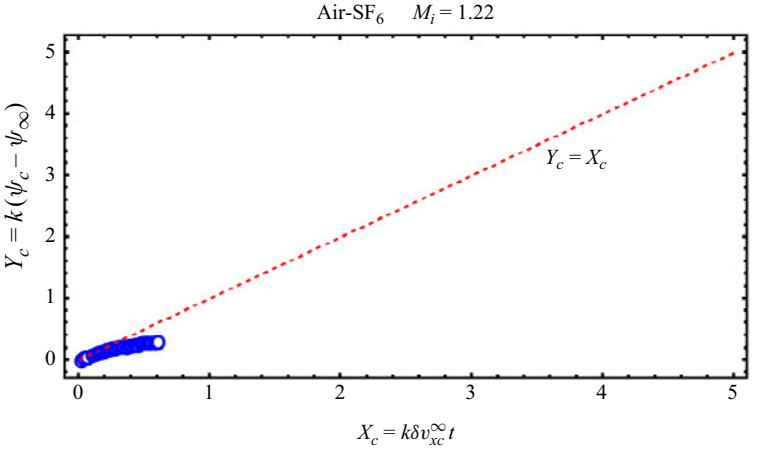


Figure 17. Reduced ripple amplitude amplitude growth for the experiments shown in figure 4 of Liu *et al.* (2018). Dashed, red line is our prediction (14.10).

As expected, nonlinear effects show up early and our formula stays well above the experimental points at large times. If we solve the equation $k\psi_c(X_i) \sim 1$, following the criterion of Vandenboomgaerde where $X_i = k\delta v_{ximp}t$, we get $X_i = \sim 3.16$, corresponding to a dimensional time $t_{NL} \sim 0.1762$s, consistent with the behaviour observed in figure 16 of this work.

15.3. *Simulations of Latini et al.* (2007)

In this subsection, we analyse the simulations of Latini *et al.* (2007), which were performed to study the experiments of Collins & Jacobs (2002). Gases are (air acetone)–SF_6, the incident sock coming from inside the mixture air(acetone). First, let us consider their initial parameters and background values for their simulations shown in figure 6(left).

The perturbation wavelength is $\lambda = 5.93333$ cm. The initial ripple amplitude is $\psi_0 = 0.2$ cm, thus giving $k\psi_0 = 0.2118 < 1$. The small parameter $k\psi_0$ is not much less than 1, meaning that nonlinear effects will show up relatively early. The authors of Latini

https://doi.org/10.1017/jfm.2025.10740 Published online by Cambridge University Press

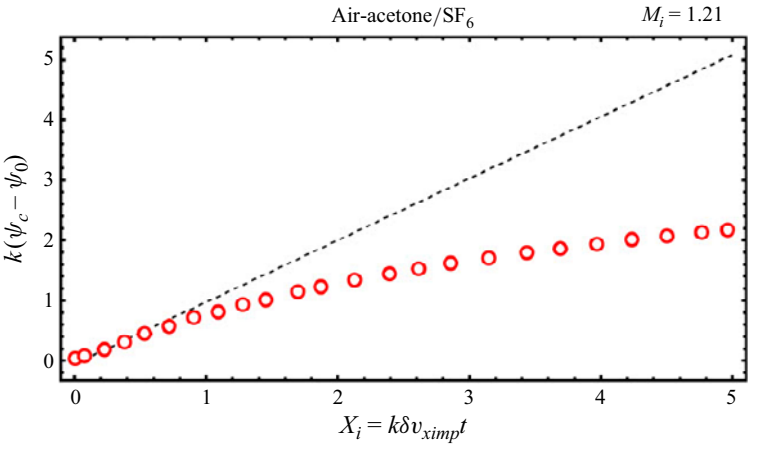


Figure 18. Ripple amplitude growth for the conditions of figure 9 of Latini *et al.* (2007).

et al. (2007) considered, for the air(acetone) mixture, $\gamma_{aa} = 1.276$, which is also the value used for the calculations here. Pre-shock density ratio and background velocities are taken from their table 1. We recall them here too for simplicity. The incident shock Mach is $M_i = 1.21$. The incident shock speed is $D_i = 36369$ cm s^{-1}, which gives us, for the velocity of the compressed contact surface, the value $U = 7669.82$ cm s^{-1}. For these conditions we get $u_c^{\infty} = 0.10369$, which gives, in dimensional units: $\delta v_{xc}^{\infty} = 799.125$ cm s^{-1}. As for the impulsive prescription, we get $\delta v_{ximp} = 1019.67$ cm s^{-1}. The impulsive model is greater than our prediction by more than 27 % despite this being a moderately weak shock ($M_i = 1.21$). An irrotational approximation, based on u_{irrot} here, gives: $\delta v_{xirrot} \sim 848.364$ cm s^{-1}. Our irrotational approximation is nearer to the exact linear theory result as it should be, given the weakness of the incident shock, and performs better than the impulsive model for these simulations.

In figure 18 we show the growth of the ripple amplitude $k(\psi_c - \psi_0)$ as a function of dimensionless time $X_i = k\delta v_{ximp}t$ for the Latini simulations (Latini *et al.* 2007). For the conditions of these simulations we get $t_{NL} \sim 0.80545$s, which is consistent with figure 18.

In figure 19 we show the reduced amplitude $k(\psi_c - \psi_\infty)$ for the simulations of Latini *et al.* (2007). The red circles are from figure 9 of Latini *et al.* (2007). The blue dashed line is the asymptotic formula given by (14.10).

In general, ψ_∞ is a small correction to either ψ_0 or ψ_0^* for very weak shocks. This behaviour is shown in figure 21.

In figure 20 we show the dependence of the offset amplitude ψ_∞ as a function of the incident shock strength for the gases indicated. The offset reaches its minimum value for a very strong incident shock, while for very weak shocks it coincides with ψ_0 and ψ_0^*.

We see that, in general, ψ_∞ is a slight correction to both ψ_0 and ψ_0^*, except for a very strong shock, a case in which ψ_∞/ψ_0 and ψ_∞/ψ_0^* reach their minimum value.

It is recalled that (14.8) must be read only for large times: at $t = 0+$, the ripple amplitude starts always from its post-shock value ψ_0^*. As time progresses and growth enters the asymptotic linear stage, well before the onset of nonlinearity, the ripple grows as if the amplitude had started from the slightly different value ψ_∞, but this is only a result valid for large times during the linear stage of growth. In Cobos-Campos & Wouchuk (2016), the authors calculated the value of ψ_∞ by iterating on the equations of Wouchuk (2001*a*). Here, thanks to (8.13), we have been able to calculate it analytically.

https://doi.org/10.1017/jfm.2025.10740 Published online by Cambridge University Press

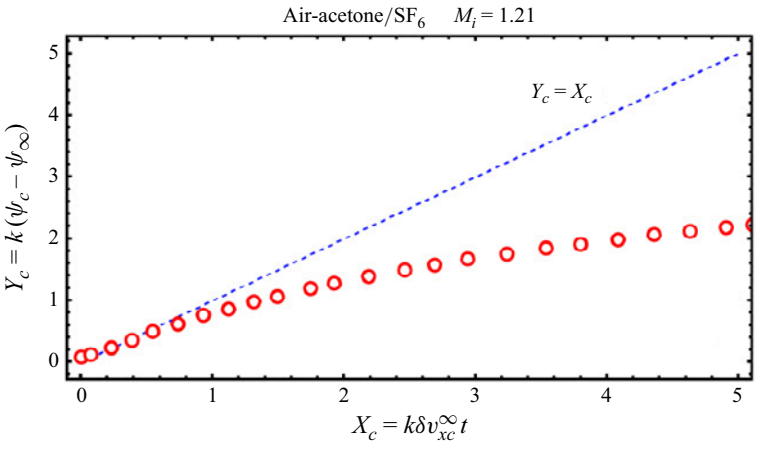


Figure 19. Reduced ripple amplitude $k(\psi_c - \psi_\infty)$ for the same conditions as in figure 18.

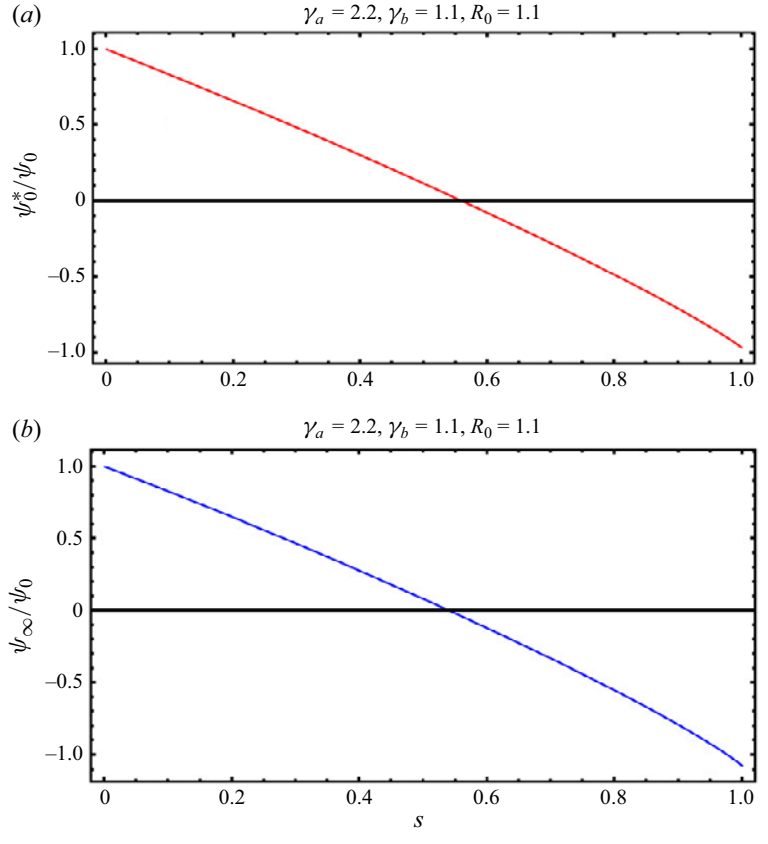


Figure 20. (*a*) Post-shock ripple amplitude ψ_0^* as a function of s, for the gases indicated. (*b*) Offset amplitude ψ_∞ as a function of s for the gases indicated.

https://doi.org/10.1017/jfm.2025.10740 Published online by Cambridge University Press

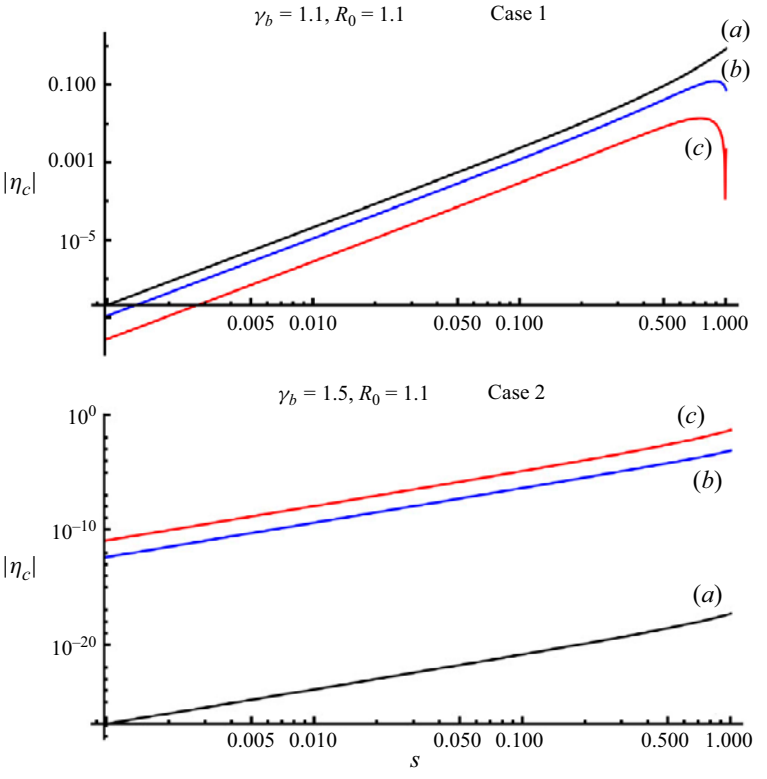


Figure 21. Absolute value of the relative error η_c as a function of the incident shock strength s for three different values of $\Gamma = \gamma_a/\gamma_b$: case 1 is for $\gamma_b = 1.1$, and case 2 is for $\gamma_b = 1.5$. Inside each case, three curves are shown for different values of the ratio $\Gamma = \gamma_a/\gamma_b$, in which black curve ($a$) has $\Gamma = 1$, black curve (b) has $\Gamma = 2$ and red curve (c) has $\Gamma = 10$.

16. Estimation of the error incurred when calculating the terminal velocity u_c^∞ because of the RPA

As we have seen before, our results for u_c^∞ deviate significantly from those published by Yang *et al.* (1994) for some regimes, especially for very strong shocks and large differences between γ_a and γ_b. It is thus mandatory for us to examine the primary sources of discrepancy. As discussed before, the main reason of discrepancy lies in the fact that our functionals (7.2, 7.5) are only approximate, because of the RPA. As the RPA may not be valid depending on which zone of the parameter space we are calculating the terminal velocity, it could be helpful to quantify, if possible, and in the most rigorous way, the relative error of the calculation shown here, as given by (9.31). The calculation of the relative error is shown soon below.

Our calculation of u_c^∞ here is based on using the solution found in § 8 for P_r, P_t. Despite the expressions found for both functions being exact solutions of the corresponding functional equations, there are intolerable differences between u_c^∞ and the results of Yang *et al.* As we have already pointed out, a main source of error lies in the prediction $F_a = 0$, because $\lambda_{a1}(\chi_t) = 0$. The reason for this contradiction is not in the solution found for P_r, P_t after (8.2), which is exact. The problem is actually the fact that the functional equations (7.2), and (7.5) themselves are approximate. They have been obtained making the important simplifications $F_{a1}(q_a) \sim F_{a2}(q_a)$, and $F_{b1}(q_b) \sim F_{b2}(q_b)$. To estimate how much our terminal velocity deviates from the exact value that would be calculated without

https://doi.org/10.1017/jfm.2025.10740 Published online by Cambridge University Press

resorting to such simplifications, let us rederive the functional equations for P_r, P_t, but allowing now for non-zero values of the differences $J_{ac}(q_a) = F_{a1}(q_a) - F_{a2}(q_a) \neq 0$ and $J_{bc}(q_b) = F_{b1}(q_b) - F_{b2}(q_b) \neq 0$. That is, in what follows, we try not to make use of the RPA. The system of functional equations shown in (Wouchuk 2001*a*) has been derived without any approximation, which explains why those results align closer to Yang *et al.* Proceeding as in § 6, we soon arrive to a corrected equation for P_t of the form

$$P_t(q_a) = \lambda_{a1}(q_a) + f_a(q_a) J_{ac}(q_a - \chi_t) + \lambda_{a2}(q_a) P_t(q_a - 2\chi_t), \tag{16.1}$$

with

$$f_a(q_a) = \frac{2}{\cosh q_a + \alpha_{a1}(q_a)}. \tag{16.2}$$

We clearly see the difference between (7.5) and (16.1): the difference stems, as expected, from the non-zero value of he function $J_{ac}(q_a)$. Proceeding similarly with the reflected shock, we get

$$P_r(q_b) = \lambda_{b1}(q_b) + \lambda_{b2}(q_b) P_r(q_b + 2\chi_r) + f_b(q_b) J_{bc}(q_b + \chi_r), \tag{16.3}$$

with

$$f_b(q_b) = \frac{2}{\alpha_{b1}(q_b) - \cosh q_b}. \tag{16.4}$$

So far, allowing for a non-zero value of $F_{m1}(q_m) - F_{m2}(q_m)$ leads us to the new (16.1, 16.3), which are 'more exact' than previous (7.2, 7.5), because the RPA is not used inside (16.1, 16.3). Let us indicate with an asterisk the solutions to (16.1, 16.3). That is, let $P_r^*(q_b)$ the solution of (16.3), and $P_t^*(q_a)$ the corresponding solution of (16.1). We define, further

$$\begin{aligned} F_a^* &= -\Omega_a \sinh \chi_t P_t^*(\chi_t), \\ F_b^* &= \Omega_b \sinh \chi_r P_r^*(\chi_r). \end{aligned} \tag{16.5}$$

Let us use the symbol u_{cex} to indicate the value of the terminal velocity that would be obtained if the RPA were not used, i.e. using F_a^* and F_b^*. Besides, we define $\Delta u = u_{cex} - u_c^\infty$ as the absolute deviation between u_{cex} and u_c^∞. The relative error is thus defined as: $\eta_c = \Delta u / u_c^\infty$. Therefore, using the above results, we can write

$$u_{cex} = u_{irrot} + \frac{R F_a^* - F_b^*}{R + 1}. \tag{16.6}$$

Noticing that $J_{ac}(0) = -u_c^\infty$ and collecting the above results we soon arrive at

$$u_{cex} = u_{irrot} + K u_c^\infty, \tag{16.7}$$

where

$$K = \frac{R \Omega_a \sinh \chi_t \; f_a(\chi_t)}{R + 1}. \tag{16.8}$$

After some additional algebra we get an expression for the relative error η_c

$$\eta_c = \frac{u_{cex} - u_c^\infty}{u_c^\infty} = L + K - 1, \tag{16.9}$$

where

$$L = -\frac{F_b^*}{(R+1) u_c^\infty}. \tag{16.10}$$

https://doi.org/10.1017/jfm.2025.10740 Published online by Cambridge University Press

The quantity F_b^* is

$$F_b^* = \Omega_b \sinh \chi_r \left[\lambda_{b1}(\chi_r) - f_b(\chi_r) J_{bc}(2\chi_r)\right]. \tag{16.11}$$

As for the value of $J_{bc}(2\chi_r)$, we use (8.13).

Having at our disposal an analytic expression for the relative error, we can study it as a function of the relevant pre-shock parameters: shock strength s, and ratio $\gamma_s'\gamma_a/\gamma_b$.

In figure 21 we show the absolute value of η_c for three different choices of $\Gamma = \gamma_a/\gamma_b$, as a function of the shock strength, for two cases: case 1, has $\gamma_b = 1.1$, while case 2, has $\gamma_b = 1.5$. As can be seen in figure 20, η_c increases monotonically from the value at $s = 0$ up to the value corresponding to a shock of infinite strength. We also analyse the behaviour of η_c as a function of $\Gamma = \gamma_a/\gamma_b$ in figure 22 for three different incident shock strengths. In figure 21, we study the relative error as a function of shock strength s for three different values of the ratio $\Gamma = \gamma_a/\gamma_b$, for two cases: case 1 has $\gamma_b = 1.1$, and case 2 has $\gamma_b = 1.5$. In both cases, the error increases toward the limit of very strong shock and shows a wide variation with the ratio of isentropic exponents Γ. Because of this, in figure 22 we study η_c as a function of Γ for three different shock strengths: very weak with $s = 1/100$, moderately weak with $s = 1/10$ and infinitely strong with $s \sim 1.0$.

In all the curves the relative error remains bounded from above. Referring to figure 21 case 1, we notice that it corresponds to a shock coming from a highly compressible fluid ($\gamma_b = 1.1$). Hence, the curve (a) with $\Gamma = 1$ corresponds to a case in which both fluids are highly compressible, which explains the large values obtained for η_c along (a). For curves (b) and (c), fluid a is much less compressible than fluid b and we get smaller values for η_c. It is important to notice that, at a given shock strength, η_c varies widely as $\Gamma = \gamma_a/\gamma_b$ is changed. This observation motivates us to show the dependence of η_c as a function of Γ at different shock strengths. This is shown in figure 22 for three different incident shock Mach numbers, for $\gamma_b = 1.1$. As expected, the largest values of $|\eta_c|$ are achieved when $s \sim 1.0$.

Figure 23 is similar to figure 22, but for a larger value of the light fluid isentropic exponent: $\gamma_b = 1.5$. At a given ratio of isentropic exponents Γ, it is clear that the error increases towards the limit $s \sim 1.0$, and, for a given shock strength, it changes gradually with Γ. In both cases of figure 22, η_c is always the highest for $s \sim 1.0$, and negligible for a very weak shock. In Yang *et al.* (1994), the authors defined a relative error $E = u_{impoulsive}/u_{sim} - 1$, where u_{sim} is thee value obtained from their simulations, to compare their simulation with the impulsive formula. This is shown in their figure 16, where they show the relative error $E(s)$, as a function of incident shock strength s for the four combinations of gases studied in that work. We obtain much lower values for the relative error E than theirs. We think this is due to the fact that in our calculation of u_c^∞ we are successfully taking into account the sound wave reverberations between the shock fronts and the contact surface, something impulsive models cannot.

It is interesting to note that curve (a) in figure 21 stays higher in case 1 than in case 2. This is reasonable because, for case 1, both gases are highly compressible as $\Gamma = 1$, i.e. $\gamma_a = \gamma_b = 1.1$.

Figure 24 shows the longitudinal component $u(x)$ of the velocity field for the pre-shock parameters indicated.

Figure 25 shows the spatial dependence of the tangential component of the velocity field $v(x)$ as a function of the longitudinal coordinate x. We see a rapid decrease like exponential decay e^{-kx} for $x \to 0$. Far from the contact surface the vorticity field dominates and the velocity oscillates in space. Such a behaviour had been also predicted by Fraley (1986).

Figure 25 shows the same for the tangential component of the velocity field, $v(x)$, as a function of the longitudinal coordinate, x. It behaves in the same way as $u(x)$.

https://doi.org/10.1017/jfm.2025.10740 Published online by Cambridge University Press

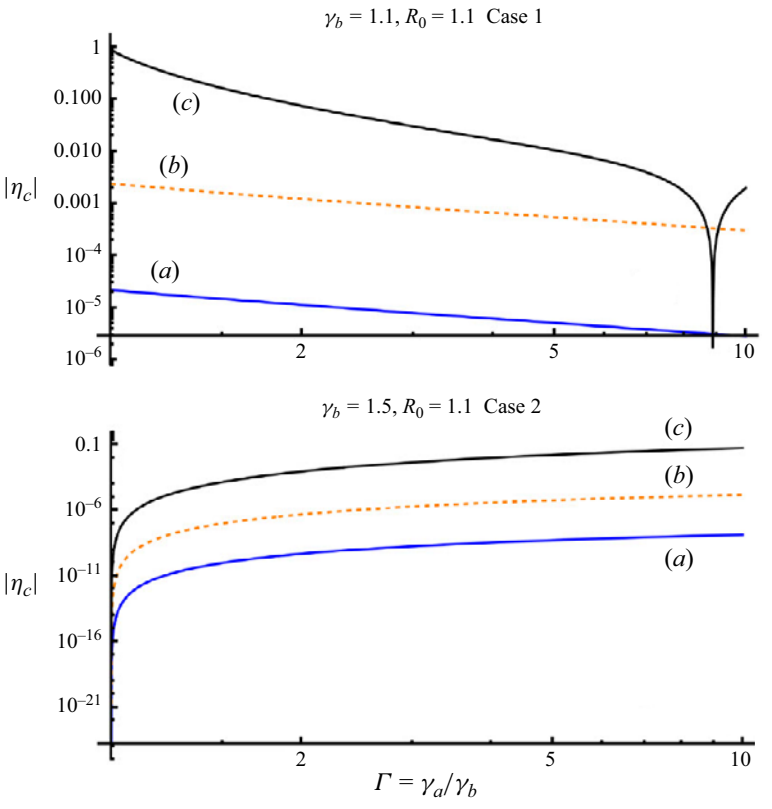


Figure 22. Value of $|\eta_c|$ as a function of Γ, for $\gamma_b = 1.1$, and three different incident shock strengths, as indicated in each panel. In each case, (a) corresponds to $s = 1/100$, (b) to $s = 1/10$ and (c) to $s \sim 1.0$.

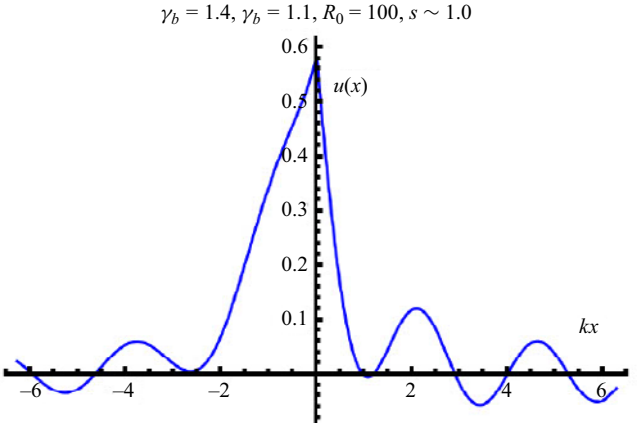


Figure 23. Longitudinal component $u(x)$ of the velocity field for the gases indicated, as function of x.

The oscillatory behaviour far from the contact surface is due to the vorticity generated by the shocks.

In figure 25 the whole velocity field in the form of a vector plot is shown for the pre-shock parameters indicated. The incident shock is very strong: $s \sim 1.0$, which corresponds in this case to $M_i \sim 30.9$. In the direction parallel to the contact surface, the velocity field

https://doi.org/10.1017/jfm.2025.10740 Published online by Cambridge University Press

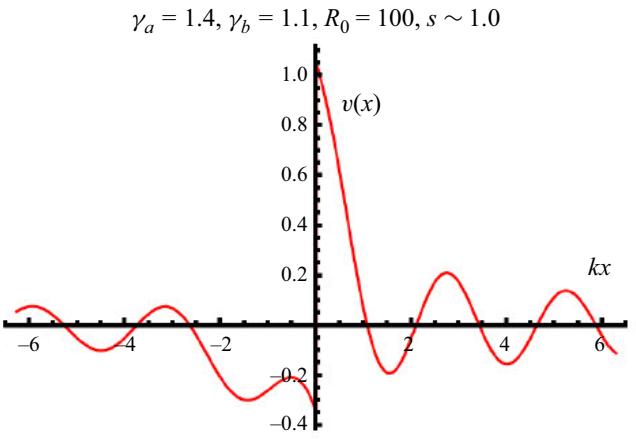


Figure 24. Tangential component $v(x)$ of the velocity field for the gases indicated, as function of x.

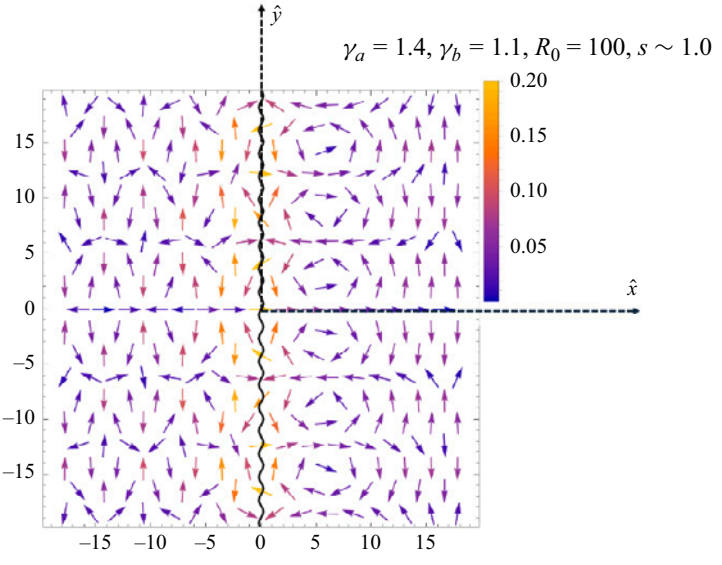


Figure 25. Vector plot of the asymptotic velocity field inside both fluids for the pre-shock parameters indicated.

spans over three wavelengths, for $y > 0$, and three wavelengths for $y < 0$. Three vortices are visible for $y > 0$, and $y < 0$. Symmetry along the x axis is not possible, because the longitudinal size of the vortices is different on each side $x > 0$, $x < 0$ because it changes with the value of γ. The size of the vortices on each side of the contact surface for the RMI problem, shock reflected case has been extensively discussed in Wouchuk & Campos (2017) and Wouchuk & Cobos-Campos (2018), where scaling laws valid in the weak shock limit have been shown.

17. Concluding remarks

Based on previous work by the author this article explores the possibility of presenting a simple analytic, albeit approximate formula for the terminal velocity of the linear RMI when a shock is reflected, as given by (9.31), using the RPA. As reported in many

https://doi.org/10.1017/jfm.2025.10740 Published online by Cambridge University Press

works before, the main difficulty in evaluating the terminal velocity comes from the bulk vorticity quantities F_a, F_b. which required elaborate calculations as in Wouchuk & Nishihara (1997), Wouchuk (2001*a*) and Cobos-Campos & Wouchuk (2016) . In this article a simplified set of equations has been obtained, embodied in (7.2, 7.5) derived after approximating the contact surface as a RPA. The RPA allows us to obtain a much simpler system of functional equations than was done in Wouchuk (2001*a*). Thanks to the analyticity of the Laplace transforms for the pressure functions, these simpler functional equations can be solved exactly providing straightforward analytical formulas for P_r and P_t, which in turn give a simpler expression for F_b. There is, however, the nuisance of the prediction $F_a = 0$, because $\lambda_{a1}(\chi_t) = 0$. This is not a problem of the method used to solve the functional equations in the complex plane , but rather in the RPA itself. The algebraic solution shown here, based on using $P_r(q_b) = \lambda_{b1}(q_b)$, $P_t(q_a) = \lambda_{a1}(q_a)$, certainly allows a straightforward calculation of the vorticity parameters F_a, F_b. However, as has been discussed before, the RPA leads us to the incorrect result $F_a = 0$, because $\lambda_{a1}(\chi_t) = 0$, which is unphysical, resulting in large values of the relative error in regimes of high compression, and/or very different γ values. This wrong result is at the heart of the disagreement observed in our table 1 when comparing with table I of Yang *et al.* (1994). Nevertheless, the reason of the wrong result $F_a = 0$ is not on the method explained in § 8 to solve the functional equations, but rather in the functional equations themselves, which have been obtained using the RPA. Nevertheless, despite this nuisance, agreement with experiments and simulations in § 15 has been shown, as those experiments and simulations have been done with relatively weak shocks. Nevertheless, agreement with Fraley's formula is certainly encouraging.

In § 16 an estimation of the relative error (η_c) incurred in calculating u_c^∞ has been done. The behaviour of η_c as a function of the shock strength and its variation by changing the ratio of γ values has been shown in figures 21, 22 and 23. The main conclusion observing the behaviour of η_c is that the prediction for the terminal velocity of this work worsens when both fluids are highly compressible, and the incident shock is infinitely strong at the same time. The algebraic solution for u_c^∞ shown here is certainly easy to implement thanks to the results of § 8. Even though the result $F_a = 0$ gives large error in some regimes, u_c^∞ compares reasonably well with experiments and simulations for relatively weak shocks. So far, an exact and analytically tractable formula for u_c^∞ is still lacking. Hopefully, the ideas presented in this work may be of help to a highly motivated post-doc/researcher elsewhere in order to find an exact, analytically tractable solution to the exact equations of Wouchuk (2001*a*), perhaps guided by the ideas of § 8.

Supplementary materials. Supplementary materials are available at https://doi.org/10.1017/jfm.2025.10740.

Acknowledgements. This work is the outgrowth of a constant effort over the last 30 years, and as such, it has benefited with enlightening discussions and encouragement from many people, among them: A.L. Velikovich ('Sasha' Velikovich, N.R.L., Washington D.C.). (H. Azechi and K. Nishihara, from I.L.E., Osaka University, Japan), (C. Matsuoka, from Osaka City University, Japan), (César Huete, from UC3M, Madrid, Spain) and (A.R. Piriz, A.C. Bret, from UCLM, Ciudad Real, Spain). Besides, the author is also grateful to J. Mingallón Martín (Ciudad Real, Spain) for assistance with some of the figures. The author would also like to especially acknowledge (K. Mikaelian, from L.L.N.L., California, USA), for interesting and stimulating discussions/suggestions regarding the results of this work, especially the calculations regarding Fraley's formula. The author is also indebted to three anonymous referees whose comments and criticisms have greatly enhanced the conclusions of this work. Last, but not least, the author is also grateful to God and to Virgin Mary for timely bursts of inspiration.

Declaration interests. The author reports no conflict of interest.

https://doi.org/10.1017/jfm.2025.10740 Published online by Cambridge University Press

References

Abramowitz, M. & Stegun, I.A. 1972 *Applied Mathematics*. Dover Publications.
Batchelor, G.K. 2002 *An Introduction to Fluid Dynamics*. Cambridge University Press.
Briscoe, M. & Kovitz, A. 1968.*J.F.M.* **31**, 297,
Calvo-Rivera, A., Velikovich, A.L. & Huete, C. 2023 *J. Fluid Mech.* **964**, A33.
Campos, F.C. & Wouchuk, J.G. 2014 *Phys. Rev. E* **90**, 053007.
Cao, Q. *et al.* 2024, *J. Fluid Mech.* **999**, A31.
Churchill, R.V. 1974 *Complex Variables and Applications*. MacGraw-Hill.
Cobos-Campos, F. & Wouchuk, J.G. 2016 *Phys. Rev. E* **93**, 053111.
Collins, B.D. & Jacobs, J.W. 2002 *J. Fluid Mech.* **464**, 113.
Dimonte, G., Frerking, C.E., Schneider, M. & Remington, B. 1996 *Phys. Plasmas* **3**, 614.
Fraley, G. 1986 *Phys. Fluids* **29**, 376.
Fu, Z. *et al.* 2025 *Phys. Plasmas* **32**, 022114.
Holmes, R.L., Dimonte, G., Bruce Fryxell, M.L.G., Grove, J.W. & Zhang, Q. 1999 *J. Fluid Mech.* **389**, 55.
Huete, C., Wouchuk, J.G., Canaud, B. & Velikovich, A.L. 2012 *J. Fluid Mech.* **700**, 214–245.
Jacobs, J.W. & Krivets, V.V. 2005 *Phys. Fluids* **17**, 034105–03.
Landau, L.D. & Lifshitz, E.M. 1986 *Fluid Mechanics*, vol. 6, Pergamon Press.
Latini, M. *et al.* 2007 *Phys. Fluids* **19**, 024104 .
Lindl, J. 2014 *Phys. Plasmas* **21**, 020501.
Liu, L., Liang, Y., Ding, J., Liu, N. & Xisheng, L. 2018 *J. Fluid Mech.* **853** (R2).
C., Matsuoka *et al.* 2003 *Phys. Rev. E* **67**, 036301–03.
Matsuoka, C. *et al.* 2020 *Phys. Plasmas* **27**, 112301.
Matsuoka, C. & Nishihara, K. 2023 *Phys. Plasmas* **30**, 062304.
Meshkov, E.E. 1969 *Fluid Dyn.* **4**, 101.
Meyer, K.A. & Blewett, P.J. 1972 *Phys. Fluids* **15**, 753.
Mikaelian, K. 1991 *Phys. Fluids* **6**,357.
Morse, P.M. & Feshbach, H. 1953 *Methods of Theoretical Physics, Part I*. Feshbach Publishing, LLC.
Napieralski, M., Cobos, F., Velikovich, A.L. & Huete, C. 2024, *J. Fluid Mech.* **A18**, 1000.
Piriz, A.R. & Wouchuk, J.G. 1992 *Nucl. Fusion* **32**, 933.
Richtmyer, R.D. 1960 *Commun. Pure Appl. Math* **13**, 297.
Sneddon, I.N. 1972 *The Use of Integral Transforms*. McGraw-Hill Book Company.
Velikovich, A.L. 1996 *Phys. Fluids* **8**, 1666.
Velikovich, A.L., Dahlburg, J.P., Schmitt, A.J., Gardner, J.H., Phillips, L.P., Cochran, F.L., Chong, Y.K., Dimonte, G. & Metzler, N. 2000 *Phys. Plasmas* **7**, 1662.
Velikovich, A.L. *et al.* 2020 *Phys. Plasmas* **27**, 102706.
Vandenboomgaerde, M., Souffland, D., Mariani, C., Biamino, L., Jourdan, G. & Houas, L. 2014 *Phys. Fluids* **26**, 024109.
Whitham, G.B.W. 1973 *Linear and Non-Linear Waves*. Wiley.
Wouchuk, J.G. 2001 *Phys. Plasmas* **8**, 2890.
Wouchuk, J.G. 2001 *Phys. Rev. E* **63**, 056303.
Wouchuk, J.G. 2025 *Phys. Rev. E* **111**, 035102–03.
Wouchuk, J.G. & Campos, F.C. 2017 *Plasma Phys. Control. Fusion* **59**, 014033.
Wouchuk, J.G. & Carretero, R. 2003 *Phys. Plasmas* **10**, 4237.
Wouchuk, J.G. & Cavada, J.L. 2004 *Phys. Rev. E* **70**, 046303.
Wouchuk, J.G. & Cobos-Campos, F. 2018 *Phys. Scr.* **93**, 094003.
Wouchuk, J.G. & Nishihara, K. 1996 *Phys. Plasmas* **3**, 3761.
Wouchuk, J.G. & Nishihara, K. 1997 *Phys. Plasmas* **4**, 1028.
Wouchuk, J.G. & Nishihara, K. 2004.
Wouchuk, J.G. & Sano, T. 2015, *Phys. Rev. E* **91**, 023005.
Yang, Y., Zhang, Q. & Sharp, D. 1994 *Phys. Fluids* **6**,1856.
Zaidel', P. 1960 *J. Appl. Math. Mech.* **24**, 316.
Zhou, Y. 2017 *Phys. Rep.* **720–722**, 1–136.
Zwillinger, D. 1983 *Handbook of Integration*. Jones and Bartlett Publishers.

https://doi.org/10.1017/jfm.2025.10740 Published online by Cambridge University Press